

1 **THIS IS A NON-PEER REVIEWED PREPRINT SUBMITTED**
2 **TO EarthArxiv**

3 **Joint inversion of co-seismic and early post-seismic slip to**
4 **optimize the information content in geodetic data: Application**
5 **to the 2009 M_w 6.3 L'Aquila earthquake, Central Italy**

6 **Théa Ragon¹, Anthony Sladen¹, Quentin Bletery¹, Mathilde Vergnolle¹, Olivier Cavalié¹,**
7 **Antonio Avallone²**

8 ¹Université Côte d'Azur, CNRS, IRD, Observatoire de la Côte d'Azur, Géoazur, Valbonne, France

9 ²Istituto Nazionale di Geofisica e Vulcanologia, Rome, Italy

10 **Key Points:**

- 11 • Simultaneous inversion of geodetic data with different spatio-temporal resolution
12 maximizes the information content
13 • Incorporating early afterslip deformation when solving for the co-seismic processes
14 (as with InSAR data) overestimate inferred co-seismic models
15 • Estimations of the post-seismic processes neglecting early afterslip deformation
16 may largely underestimate the total afterslip amplitude

Corresponding author: Théa Ragon, ragon@geoazur.unice.fr

Abstract

When analyzing the rupture of a large earthquake, geodetic data are often critical. These data are generally characterized by either a good temporal or a good spatial resolution, but rarely both. As a consequence, many studies analyze the co-seismic rupture with data also including one or more days of early post-seismic deformation. Here, we propose to invert simultaneously for the co- and post-seismic slip with the condition that the sum of the two models remains compatible with data covering the two slip episodes. We validate the benefits of our approach with a toy model and an application to the 2009 M_w 6.3 L'Aquila earthquake, using a Bayesian approach and accounting for epistemic uncertainties. For the L'Aquila earthquake, we find that if early post-seismic deformation is acknowledged as co-seismic signal, co-seismic slip models may overestimate the peak amplitude while long-term post-seismic models may largely underestimate the total post-seismic slip amplitude. This example illustrates how the proposed approach could improve our comprehension of the seismic cycle, of the fault frictional properties, and how the co-seismic rupture, afterslip and aftershocks relate to one another.

1 Introduction

The occurrence of earthquakes and seismic sequences is mainly controlled by the spatial and temporal evolution of crustal stresses. The co-seismic stress change and the redistribution of stress following an earthquake thus both play an important role in the seismic cycle and the mechanical behavior of faults, including the generation of new seismic sequences. To understand both co-seismic and post-seismic processes, and their relationship, is thus a crucial step to propose realistic earthquakes scenario and reliable hazards estimates.

While earthquakes can last for a few seconds to minutes, their post-seismic stress relaxation can last months to years. Post-seismic relaxation is generally modeled by several interacting mechanisms, such as localized shear on the fault (a.k.a. afterslip) [e.g. *Marone et al.*, 1991; *Freed*, 2007; *Johnson et al.*, 2012], visco-elastic deformation in the lower crust or mantle [e.g. *Nur and Mavko*, 1974; *Pollitz et al.*, 1998; *Freed and Burgmann*, 2004] or poroelastic rebound [e.g. *Peltzer et al.*, 1998; *Jonsson et al.*, 2003]. The interactions between co-seismic stress changes, aftershocks and post-seismic deformation are still poorly understood [e.g. *Perfettini and Avouac*, 2007]. Slip on the fault may be governed by two brittle deformation modes following rate and state friction laws [*Rice and L. Ruina*, 1983]: seismic rupture may occur in velocity weakening area, whereas afterslip may develop in the velocity strengthening zone [e.g. *Marone et al.*, 1991]. In contrast, *Helmstetter and Shaw* [2009] also show that afterslip processes may be primarily driven by stress heterogeneities, independently of the rate and state friction behavior. Aftershocks may be triggered by co-seismic stress changes, without direct relation with post-seismic deformation [*Dieterich*, 1994]. Or, aftershocks may also be primarily triggered by the post-seismic reloading due to afterslip [e.g. *Perfettini and Avouac*, 2004; *Hsu et al.*, 2006; *Peng and Zhao*, 2009; *Ross et al.*, 2017]. The variability of these theories emphasizes the need to refine our comprehension and description of the co-seismic and post-seismic phases and their transition.

Our understanding of the co-seismic processes mainly derives from modeling of seismic, geodetic and tsunami data, and our understanding of post-seismic behaviors is mainly improved with the modeling of geodetic observations [e.g. *Burgmann et al.*, 1997; *Wang et al.*, 2012; *Perfettini and Avouac*, 2014; *Gualandi et al.*, 2017] or simulation [e.g. *Smith and Sandwell*, 2004; *Barbot and Fialko*, 2010; *Cubas et al.*, 2015]. The observations thus remain a cornerstone to identify and characterize the co- and post-seismic processes. GNSS time series are commonly used and can provide a good temporal resolution. But the spatial resolution of such observation is usually limited. In contrast, synthetic aperture radar interferometry (InSAR) can provide extensive spatial coverage but with a limited

temporal resolution. Indeed, while earthquakes last for a few seconds, very often satellites have a revisit time of more than a few days. If earthquakes do not nucleate just before the visit of a satellite, which is generally the case, the measured deformation is the co-seismic signal plus a fraction of the post-seismic deformation. As a consequence, most earthquakes models based on geodetic observations are biased by unwanted deformation signal. In practice, used interferograms or campaign GNSS offsets generally cover time periods extending at least a few days before and after the mainshock. Pre-earthquake signals, when evidenced, are usually related to small slip episodes at depth near the hypocenter. The associated surface deformation signals are usually hard to detect and neglected in co-seismic studies. The post-seismic deformation happening on the first few days after the mainshock is usually detectable in the geodetic data but incorporated in source estimation problems as if it was part of the co-seismic signal [e.g. *Elliott et al.*, 2013; *Lin et al.*, 2013; *Cheloni et al.*, 2014; *Bletery et al.*, 2016; *He et al.*, 2017; *Salman et al.*, 2017; *Barnhart et al.*, 2018], with the justification that it is comparatively small. Similarly, post-seismic models generally do not account for observations related to the early post-seismic deformation because they are often contaminated by co-seismic signal [e.g. *D'Agostino et al.*, 2012; *Cheloni et al.*, 2014]. What we name here the early post-seismic phase corresponds to the overlooked part of the post-seismic deformation, and can last for a few hours after the mainshock in the best case, or a few days in most studies. Yet, the largest post-seismic deformation rate is expected during the first few days after the mainshock, considering that its main trend is to decrease exponentially with time after an earthquake.

The early post-seismic processes remain largely unexplored, because of the limited temporal and spatial resolution of geodetic data. Neglecting the early post-seismic signal may also affect our understanding of both co-seismic and post-seismic processes. And this effect is probably persisting if seismic data (i.e. purely co-seismic) are added to the inverse problem, since geodetic data tend to have a stronger control on the inferred distribution of slip, at least in the first 10 km below the Earth surface [e.g. *Delouis et al.*, 2002].

The recent advent of high-frequency GNSS has allowed to record the strictly co-seismic signal (10 to 30 seconds after the earthquake time occurrence) without any contamination by early post-seismic deformation. Well instrumented earthquakes are thus now characterized by at least two geodetic datasets, one being strictly co-seismic and the other which also includes some days of early afterslip. In this study, we use an original inversion methodology to jointly infer co-seismic and early post-seismic slip models, taking advantage of the complementary spatial and temporal resolutions of different geodetic observations. We first validate the approach through a toy model, and then analyze and illustrate the benefits of our methodology with a real event. We consider the 2009 M_w 6.3 L'Aquila earthquake, Central Italy, which has been intensively studied but whose very early post-seismic phase has not been imaged. The choice of the L'Aquila event is also motivated by the large density of near field observations and the overall quality of the instrumentation. Additionally, this event ruptured a relatively well known and simple fault geometry, in an area where crustal properties have been investigated in detail: this will ensure the forward physics and its uncertainties can be estimated. In this work we investigate the impact of accounting for early afterslip on co-seismic models. We explore the impact of uncertainties in the slip imagery with a probabilistic approach and account for uncertainties in the physics of our problem. The results will allow us to investigate the relationship between co-seismic rupture, early afterslip processes, longer term afterslip and the distribution of aftershocks.

2 Inversion Framework

2.1 Dual time inversion of co-seismic and early post-seismic data

For a number of earthquakes, we have the opportunity to use two static datasets: one which is strictly co-seismic ("co") and the other which contains co-seismic and early

119 post-seismic signal ("co+post"). To infer the strictly co-seismic and early post-seismic
 120 slip distributions, one approach could be to invert separately for the two datasets, and as-
 121 sume that the strictly post-seismic ("post") solution is the difference between the "co" and
 122 "co+post" models. However, in this case, the model "co" would be constrained by fewer
 123 observations (only few GNSS offsets), most of the co-seismic information being in the
 124 "co+post" dataset (dense map of InSAR offsets). An alternative approach is to assume
 125 that the "co+post" slip model is the sum of the "co" and "post" slip distributions. We then
 126 have:

$$\begin{cases} \mathbf{d}_{\text{co}} = \mathbf{G}_{\text{co}}^{\text{co}} \cdot \mathbf{m}_{\text{co}} \\ \mathbf{d}_{\text{co+post}} = \mathbf{G}_{\text{co+post}}^{\text{co}} \cdot \mathbf{m}_{\text{co}} + \mathbf{G}_{\text{co+post}}^{\text{post}} \cdot \mathbf{m}_{\text{post}} \end{cases} \quad (1)$$

127 where matrices of the Green's functions $\mathbf{G}_{\text{data}}^{\text{model}}$ have been calculated for the corresponding
 128 dataset and model. For instance, $\mathbf{G}_{\text{co+post}}^{\text{co}}$ is the matrix of the Green's functions calculated
 129 from the model "co" for the data "co+post". The Eq. 1 can also be represented in the fol-
 130 lowing matrix form:

$$\begin{pmatrix} \mathbf{d}_{\text{co}} \\ \mathbf{d}_{\text{co+post}} \end{pmatrix} = \begin{pmatrix} \mathbf{G}_{\text{co}}^{\text{co}} & 0 \\ \mathbf{G}_{\text{co+post}}^{\text{co}} & \mathbf{G}_{\text{co+post}}^{\text{post}} \end{pmatrix} \cdot \begin{pmatrix} \mathbf{m}_{\text{co}} \\ \mathbf{m}_{\text{post}} \end{pmatrix}. \quad (2)$$

131 The redesigned Green's functions matrix is now composed of 3 sub-matrices. As we fo-
 132 cus on the early post-seismic phase, we can make the assumption that both $\mathbf{G}_{\text{co+post}}^{\text{co}}$ and
 133 $\mathbf{G}_{\text{co+post}}^{\text{post}}$ matrices are identical because we suppose both co-seismic and early post-seismic
 134 deformations are elastic. We can thus write

$$\begin{pmatrix} \mathbf{d}_{\text{co}} \\ \mathbf{d}_{\text{co+post}} \end{pmatrix} = \begin{pmatrix} \mathbf{G}_{\text{co}} & 0 \\ \mathbf{G}_{\text{co+post}} & \mathbf{G}_{\text{co+post}} \end{pmatrix} \cdot \begin{pmatrix} \mathbf{m}_{\text{co}} \\ \mathbf{m}_{\text{post}} \end{pmatrix}. \quad (3)$$

135 If strictly post-seismic observations are available, we could also incorporate these data into
 136 our equation to help constrain the "post" model:

$$\begin{pmatrix} \mathbf{d}_{\text{co}} \\ \mathbf{d}_{\text{co+post}} \\ \mathbf{d}_{\text{post}} \end{pmatrix} = \begin{pmatrix} \mathbf{G}_{\text{co}}^{\text{co}} & 0 \\ \mathbf{G}_{\text{co+post}}^{\text{co}} & \mathbf{G}_{\text{co+post}}^{\text{post}} \\ 0 & \mathbf{G}_{\text{post}}^{\text{post}} \end{pmatrix} \cdot \begin{pmatrix} \mathbf{m}_{\text{co}} \\ \mathbf{m}_{\text{post}} \end{pmatrix}, \quad (4)$$

137 with $\mathbf{G}_{\text{post}}^{\text{post}}$ reflecting the response of the Earth for the strictly post-seismic data. The "post"
 138 dataset then corresponds to the same post-seismic time window as what is covered by the
 139 "co+post" dataset.

140 The off-diagonal terms of the redesigned Green's function matrix allow us to make
 141 use of the "co+post" dataset to constrain both "co" and "post" models. In the following,
 142 we refer to this approach as Combined Time Windows (CTW) approach. The CTW ap-
 143 proach can be generalized to cover various intervals of post-seismic deformation. Indeed,
 144 while for many earthquakes strictly co-seismic data are now available, non-strictly co-
 145 seismic datasets usually cover variable time intervals. If, for instance, two intervals of
 146 post-seismic deformation contaminate the co-seismic signal, with only one of these in-
 147 tervals observed independently, our equation 3 can be adapted as

$$\begin{pmatrix} \mathbf{d}_{\text{co}} \\ \mathbf{d}_{\text{co+post1}} \\ \mathbf{d}_{\text{co+post2}} \\ \mathbf{d}_{\text{post2}} \end{pmatrix} = \begin{pmatrix} \mathbf{G}_{\text{co}}^{\text{co}} & 0 & 0 \\ \mathbf{G}_{\text{co+post1}}^{\text{co}} & \mathbf{G}_{\text{co+post1}}^{\text{post1}} & 0 \\ \mathbf{G}_{\text{co+post2}}^{\text{co}} & \mathbf{G}_{\text{co+post2}}^{\text{post1}} & \mathbf{G}_{\text{co+post2}}^{\text{post2}} \\ 0 & 0 & \mathbf{G}_{\text{post2}}^{\text{post2}} \end{pmatrix} \cdot \begin{pmatrix} \mathbf{m}_{\text{co}} \\ \mathbf{m}_{\text{post1}} \\ \mathbf{m}_{\text{post2}} \end{pmatrix}, \quad (5)$$

148 with $\mathbf{d}_{\text{post2}}$ reflecting the surface displacement for the time interval between times 1 and
 149 2, and $\mathbf{G}_{\text{post2}}^{\text{post2}}$ and $\mathbf{m}_{\text{post2}}$ associated Green's functions and slip model. Indeed, this ap-
 150 proach could be used to investigate as many time windows of post-seismic deformation
 151 as needed.

152 To refine co-seismic models and investigate early post-seismic deformation of the
 153 L'Aquila earthquake, we follow here the approach described by Eqs 1 and 3. We do not
 154 incorporate any information on the strictly post-seismic phase to investigate the very sim-
 155 ple case where only co-seismic data (contaminated or not by early post-seismic deforma-
 156 tion) are available.

157 2.2 Accounting for Epistemic Uncertainties

158 When imaging a slip distribution on a fault, the physics of the forward model is
 159 usually assumed of minimum complexity to simplify the computation and also often be-
 160 cause we don't know well the Earth interior. For instance, Earth interior is frequently ap-
 161 proximated as an elastic and homogeneous environment and the causative fault geometry
 162 is usually reduced to a flat rectangular plane. The uncertainties related to our approxima-
 163 tions of the physics of the Earth affect the inferred source models [Ragon *et al.*, 2018].
 164 As the early post-seismic slip is of limited amplitude, it may be particularly impacted by
 165 uncertainties of the forward model. We thus account for epistemic uncertainties following
 166 the approach developed by Duputel *et al.* [2014] for the Earth elastic properties and Ragon
 167 *et al.* [2018] for the fault geometry. The epistemic uncertainties are calculated from the
 168 sensitivity of the Green's Functions and are included in a covariance matrix \mathbf{C}_p .

169 2.3 Bayesian approach

170 Our inverse problem solves for both co-seismic and early post-seismic slip param-
 171 eters, the later being of limited amplitude. While the co-seismic parameters will be rea-
 172 sonably well constrained, multiple early post-seismic models will probably be realistic.
 173 To get a robust image of the early post-seismic phase, we thus solve our problem with
 174 a Bayesian sampling approach which relies on the AITar package, which is a rewrite of
 175 the code CATMIP [Minson *et al.*, 2013]. AITar combines the Metropolis algorithm with a
 176 tempering process to realize an iterative sampling of the solution space of the source mod-
 177 els. A large number of samples are tested in parallel at each transitional step. Addition-
 178 ally, a resampling is performed at the end of each step to replace less probable models.
 179 The probability of each sample to be selected depends on its ability to fit the observations
 180 \mathbf{d}_{obs} within the uncertainties $\mathbf{C}_\chi = \mathbf{C}_d + \mathbf{C}_p$, with \mathbf{C}_d the observational errors and \mathbf{C}_p the
 181 epistemic uncertainties.

182 The ability of each model parameter to solve the source problem is evaluated through
 183 repeated updates of the probability density functions (PDFs)

$$f(\mathbf{m}, \beta_i) \propto p(\mathbf{m}) \cdot \exp[-\beta_i \cdot \chi(\mathbf{m})], \quad (6)$$

184 where \mathbf{m} is the current sample, $p(\mathbf{m})$ is the prior information on this sample, i corre-
 185 sponds to each iteration and β evolves dynamically from 0 to 1 to ensure an exhaustive
 186 exploration of the solution space [Minson *et al.*, 2013]. $\chi(\mathbf{m})$ is the misfit function:

$$\chi(\mathbf{m}) = \frac{1}{2} [\mathbf{d}_{\text{obs}} - \mathbf{G} \cdot \mathbf{m}]^T \cdot \mathbf{C}_\chi^{-1} \cdot [\mathbf{d}_{\text{obs}} - \mathbf{G} \cdot \mathbf{m}]. \quad (7)$$

187 The use of AITar with the CTW approach allows us to specify prior information on each
 188 model, and thus to ensure the non-negativity of both co-seismic and post-seismic slip
 189 models (or of any time window model).

190 3 Application to a simplified 2D model

191 To ensure that our methodology allows to reliably infer the slip distribution of dif-
 192 ferent time windows, we first analyze a synthetic 2D case where the slip is imaged either

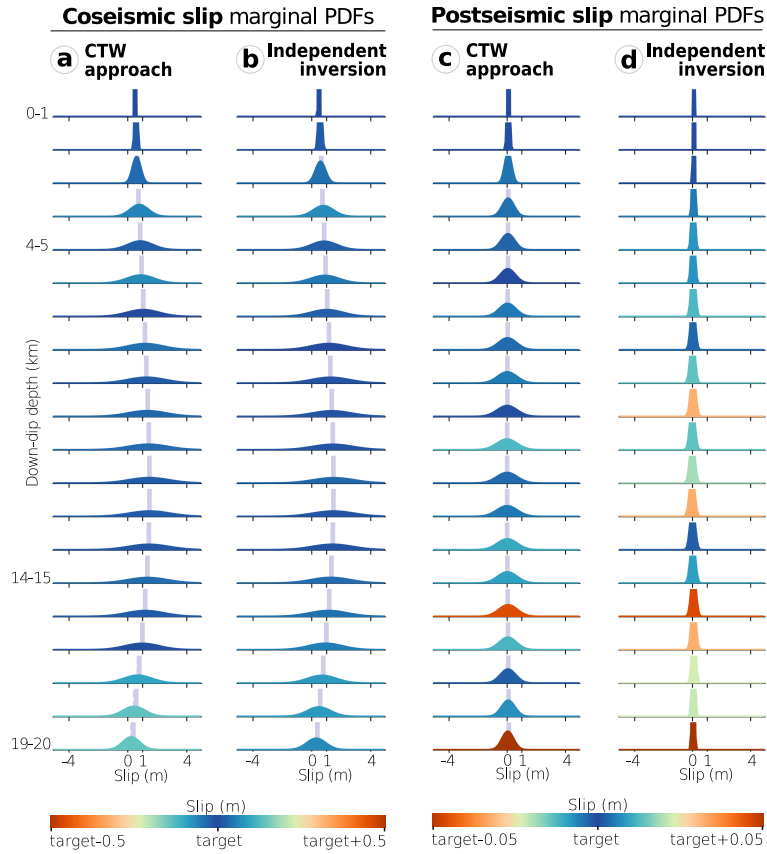


Figure 1. Co-seismic and post-seismic slip inferred for the simplified case of a fault that extends infinitely along strike. The co- and post-seismic slip models inferred from the CTW approach are shown in (a) and (c), and can be compared to the slip inferred from the inversion of co-seismic data only (b) and the post-seismic slip distribution (d) resulting from the difference between slip inferred from the inversion of co+post data and slip of (b). The fault is discretized along dip in 20 subfaults, for which are represented the target parameters as gray vertical lines. For each subfault, the posterior PDFs of co-seismic (a and b) and post-seismic (c and d) slip is colored according to the offset between the target parameter and the posterior mean, with a colorscale saturated at 50 cm for the co-seismic slip and at 5 cm for the post-seismic slip. The target slip is well inferred if the PDF of a particular parameter is colored in dark blue, while it is not if the PDF is colored in red.

193 independently or with the CTW approach. For this simple case, we assume two time win-
 194 dows named for the purpose of simplicity co-seismic and post-seismic.

195 3.1 Forward Model

196 We assume a fault extending infinitely along strike and which is 20 km wide along
 197 dip. The fault is discretized along dip into sub-faults of 1 km width and is dipping 55° .
 198 We assume the co-seismic slip on this fault to be purely dip-slip and to vary gradually
 199 with depth between 0 m and 1.5 m, with maximum slip between 9 and 14 km depth. We
 200 also assume that there is post-seismic slip on the same fault, with a similar location and
 201 direction and an amplitude equal to a tenth of the co-seismic slip amplitude. We compute
 202 the corresponding "co" and "co+post" synthetic observations using the expressions of sur-
 203 face displacement in an homogeneous elastic half-space [Segall, 2010]. These synthetic
 204 observations are computed for 100 data points at the surface, spaced every kilometer. A

205 correlated Gaussian noise of 5 mm is added to the synthetic data to simulate measurement
 206 errors. Note that, for this toy model, the number of "co" data is the same as the number
 207 of "co+post" observations.

208 Using these 100 synthetic observation points, we then estimate the depth distribu-
 209 tion of slip still assuming a homogeneous elastic half-space. We use a uniform prior dis-
 210 tribution $p(\mathbf{m}) = \mathcal{U}(-0.5 \text{ m}, 5 \text{ m})$ for the dip slip component (uniform implies that all
 211 values are considered equally likely with no a priori knowledge), a zero-mean Gaussian
 212 prior $p(\mathbf{m}) = \mathcal{N}(-0.1 \text{ m}, 0.1 \text{ m})$ on the strike-slip component and include 5 mm of obser-
 213 vational uncertainty in \mathbf{C}_d . We do not account for epistemic uncertainties as our forward
 214 model is the replicate of the one used to generate the data. We first solve for the "co" and
 215 "post" slip following the CTW approach (Figures 1a and 1c). Then, we run independent
 216 inversions, one to solve for the "co" slip and the other one to infer the "co+post" slip, the
 217 post-seismic solution being the difference between "co" and "co+post" models (Figures 1b
 218 and 1d).

219 3.2 Results

220 Both independent and CTW inversion approaches allow to correctly infer the "co"
 221 slip, as the median of the PDFs is very close to the target model (Figures 1a and 1b). As
 222 expected from the inversion of surface data, the resolution is very good on shallow parts
 223 of the fault but quickly decreases with depth. The posterior uncertainty on deepest param-
 224 eters is slightly decreased because the lower tip of the fault acts as an additional constrain.
 225 In contrast, the inversion methodology has a larger impact on the inferred "post" slip dis-
 226 tributions. When jointly inverting "co" and "co+post" observations, the correct "post" slip
 227 is well estimated at almost all subfaults (Figure 1c). When solving the two slip stages sep-
 228 arately, the mean of the models is not as good at estimating the target model (Figure 1d).
 229 The reduced posterior uncertainty of the "post" model for the independent inversion is an
 230 artifact resulting from the subtraction of two gaussian-shaped curves.

231 In summary, the two inversion approaches allow to reliably infer the "co" slip dis-
 232 tributions, probably because its signal is dominating in the observations. But the CTW
 233 approach provides a more robust estimation of the "post" slip distribution. In this 2D case,
 234 co-seismic and co+post signals have been observed by the same number of stations. How-
 235 ever, for most earthquakes, the number of "co" data points available (usually GNSS) will
 236 be very limited compared to the quantity of "co+post" observations (usually InSAR). We
 237 thus expect that if performing independent inversions for a real event, the inferred "co"
 238 slip distribution will be less reliable than in the case of a CTW inversion, where the whole
 239 "co+post" dataset is used to guide the choice of co-seismic parameters. We now compare
 240 these two approaches on a real earthquake.

241 4 Application to the 2009 M_w 6.3 L'Aquila earthquake, Central Italy

242 The L'Aquila earthquake nucleated within the Apennines orogenic system (Fig-
 243 ure 2), where the current seismic activity results from the ongoing extensional tectonics
 244 of the area. The mainshock nucleated on the Paganica fault [Figure 2, *Atzori et al.*, 2009;
 245 *Falucci et al.*, 2009; *Chiaraluca et al.*, 2011; *Vittori et al.*, 2011; *Lavecchia et al.*, 2012;
 246 *Cheloni et al.*, 2014], southwest of the city of L'Aquila, and has been followed by at least
 247 4 aftershocks of $M_w > 5$ [*Scognamiglio et al.*, 2009; *Chiarabba et al.*, 2009; *Pondrelli*
 248 *et al.*, 2010]. Although the L'Aquila earthquake has been intensively studied, most co-
 249 and post-seismic models have considered the first days of post-seismic deformation as if
 250 they were part of the co-seismic phase [e.g. *Anzidei et al.*, 2009; *Atzori et al.*, 2009; *Cheloni*
 251 *et al.*, 2010; *Trasatti et al.*, 2011; *Cirella et al.*, 2012; *D'Agostino et al.*, 2012; *Cheloni*
 252 *et al.*, 2014; *Balestra and Delouis*, 2015; *Volpe et al.*, 2015]. To avoid the contamination of
 253 co-seismic signal by early afterslip, *Yano et al.* [2014] proposed to explore independently
 254 the early post-seismic deformation, yet with datasets covering different time intervals (1

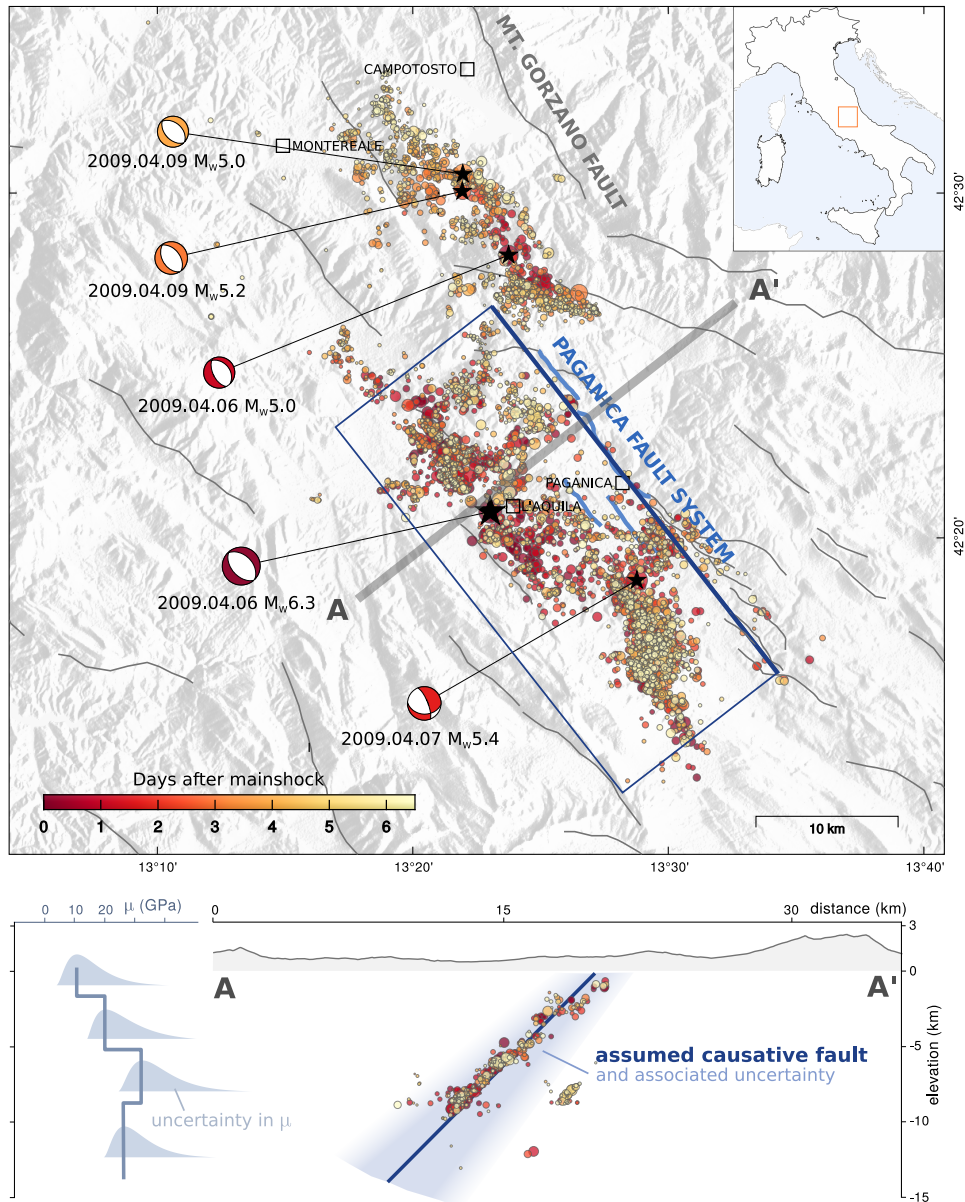


Figure 2. Seismotectonic framework of the area involved in the 2009 seismic sequence (top) and assumed forward model and associated uncertainties (bottom). In the map, coloured circles are the aftershocks from 2009 April 6 at 01:32 UTC to 2009 April 12, from the catalog of *Valoroso et al.* [2013]. The aftershocks are coloured from their occurrence time after the mainshock. Beach balls are the focal mechanisms of the mainshock and four main aftershocks, with their respective epicenters located by black stars. Solid gray lines are the major seismogenic faults of the area [*Boncio et al.*, 2004a; *Lavecchia et al.*, 2012]. The observed co-seismic surface rupture is indicated with continuous blue lines [*Boncio et al.*, 2010]. Our assumed fault geometry is shown with a dark blue rectangle. In the elevation profile (bottom), uncertainty in the fault geometry is illustrated in blue. The assumed elastic modulus μ and associated uncertainties are also illustrated for the 12 first kilometers below the Earth surface.

256 ment is recorded up to several months after the mainshock [e.g. *D'Agostino et al.*, 2012;
 257 *Gualandi et al.*, 2014; *Cheloni et al.*, 2014; *Albano et al.*, 2015], yet most studies of long-
 258 term post-seismic signal did not analyze the first few days of post-seismic deformation.

259 **4.1 Data, Forward Model and Prior Information**

260 From a geodetic perspective, this event has been particularly well documented. We
 261 can distinguish two main static datasets: one which is strictly co-seismic ("co", using con-
 262 tinuous GNSS data), and the other which also includes some days of post-seismic slip
 263 ("co+post", using cGNSS and InSAR). Two SAR images were acquired 6 days after the
 264 mainshock rupture, making the L'Aquila earthquake a perfect case study for our proposed
 265 approach. The "co" dataset corresponds to surface displacements measured between the
 266 earthquake time occurrence (t_0) and 25-30 s after t_0 , and includes the static offsets of 41
 267 (including high-rates) GPS stations surrounding the earthquake area processed by *Aval-*
 268 *lone et al.* [2011]. The "co+post" dataset covers the co-seismic phase plus 6 days of post-
 269 seismic slip, documented by 40 static GPS offsets and 2 InSAR frames: an ascending
 270 COSMO-SkyMed frame and a descending Envisat frame (Tab. S1). The observations and
 271 their processing are detailed in Supplementary Material [Section S1, *Rosen et al.*, 2004;
 272 *Lohman and Simons*, 2005; *Jolivet et al.*, 2012].

273 The Paganica fault is generally thought to be responsible for the co-seismic rupture
 274 of the L'Aquila earthquake, and also for most of its post-seismic deformation [*D'Agostino*
 275 *et al.*, 2012; *Cheloni et al.*, 2014; *Yano et al.*, 2014] along with the northernmost Cam-
 276 potosto fault [Figure 2, *Gualandi et al.*, 2014]. Although the distribution of relocalized
 277 aftershocks and surface rupture suggest that the Paganica fault system is possibly seg-
 278 mented [*Boncio et al.*, 2010; *Lavecchia et al.*, 2012] and/or curved at depth [*Chiaralu-*
 279 *ce et al.*, 2011; *Lavecchia et al.*, 2012; *Valoroso et al.*, 2013], its geometry remains poorly
 280 constrained below the surface. The variability of published morphologies for the causative
 281 fault [*Lavecchia et al.*, 2012] suggests that even with a large amount of observations and a
 282 great seismotectonic knowledge of the area, it is not possible to determine a unique fault
 283 geometry. This is why we approximate the Paganica fault geometry as a planar surface.
 284 We determine strike and position from the trace of the co-seismic surface rupture [*EMER-*
 285 *GEO Working Group*, 2010; *Boncio et al.*, 2010] and formerly identified seismogenic faults
 286 [e.g. *Boncio et al.*, 2004b]. We select the dip and width based on aftershocks relocations
 287 and focal mechanisms [e.g. *Chiaralu-*
 288 *ce et al.*, 2011; *Chiaralu-*
 289 *ce*, 2012; *Valoroso et al.*,
 290 2013]. Hence, our preferred geometry extends over 25 km south of coordinates (13.386°
 291 E, 42.445° N) with a strike of N142°. We set fault dip at 54° and width at 18 km, such
 292 that the fault is reaching the ground surface. This geometry is in agreement with already
 293 proposed causative structures [e.g. *Lavecchia et al.*, 2012]. The fault is divided into 154
 294 subfaults of 1.8 km length and 1.6 km width. As our fault geometry does not reflect the
 295 reality and is poorly constrained, we account for its uncertainties [*Ragon et al.*, 2018] and
 assume a standard deviation on the fault dip of 5° and on the fault position of 1.5 km,
 regarding the discrepancies between published fault models [e.g. *Lavecchia et al.*, 2012].

296 We perform the static slip inversion assuming a 1-D layered elastic structure de-
 297 rived from the CIA velocity model [*Herrmann et al.*, 2011], and calculate Green's func-
 298 tions with the EDKS software [*Zhu and Rivera*, 2002]. We precompute Green's functions
 299 at depths intervals of 500 m down to 15 km depth and every 5 km below. Laterally, the
 300 Green's functions are computed every kilometer to reach the maximum epicentral distance
 301 of 100 km. Then, we interpolate and sum pre-computed Green's functions given our fault
 302 geometry and data locations. The strong variability in published elastic models for the
 303 central Italy [*Herrmann et al.*, 2011] can have a strong influence on co-seismic slip esti-
 304 mates [e.g. *Trasatti et al.*, 2011; *Volpe et al.*, 2012; *Gallovic et al.*, 2015]. We thus account
 305 for the uncertainties in our Earth model [*Duputel et al.*, 2014] assuming a standard devia-
 306 tion on shear modulus of 4 % at depths greater than 15 km and 13 % above. These values

307 have been chosen a priori considering the variability between layered models and the hori-
 308 zontal variability of 3D crustal models for several depth intervals [*Magnoni et al.*, 2014].

309 We perform our static slip inversion as previously detailed in Section 2. We specify
 310 prior distributions for each model parameter: a zero-mean Gaussian prior $p(\mathbf{m}) = \mathcal{N}(-10$
 311 cm, 10 cm) on the strike-slip component (we assume that, on average, the slip direction is
 312 along dip) and we consider each possible value of dip-slip displacement equally likely if
 313 it does not exceed 20 cm of reverse slip and 5 m of normal slip: $p(\mathbf{m}) = \mathcal{U}(-20$ cm, 500
 314 cm).

315 4.2 Co-seismic and early post-seismic slip models

316 We will start by analyzing models inferred by the independent approach as applied
 317 to the two datasets. The first model is inferred from "co" data (model COgps) and the
 318 second is estimated from the "co+post" dataset (model COPOST). The "co+post" dataset
 319 is similar to what has been used in several previous studies to infer the co-seismic slip
 320 [*Cirella et al.*, 2012; *D'Agostino et al.*, 2012; *Cheloni et al.*, 2014; *Yano et al.*, 2014; *Volpe*
 321 *et al.*, 2015]. The results of these two inversions will then be compared to those of the
 322 CTW inversion. For the sake of comparison, these inversions are performed without ac-
 323 counting for epistemic uncertainties. This refinement will only be added in a final inver-
 324 sion.

325 For each approach, the results are a set of 300,000 models corresponding to the
 326 most plausible samples of the full solution space whose interpretation can provide nu-
 327 merous information: posterior uncertainty of the parameters, trade-off between parameters
 328 of the model, entropy of our model, etc. As we are tied to the need of presenting our re-
 329 sults with 2D figures when the exploration is done on a parameter space of tenth of di-
 330 mensions, we choose to represent our results in 3 different ways. In the main manuscript,
 331 the first representation illustrates the relations between neighboring subfaults and the vari-
 332 ability of most probable parameters. To do so, we divide our models into 25 families, and
 333 represent the median model of each family in different pixels in each subfault (e.g. Fig-
 334 ures 3a-d, 5a-b). A selected model will be added to the first family if it is equal to the
 335 median of the 300,000 models within a tolerance of 50 cm (for each co-seismic parame-
 336 ter) or 25 cm (for post-seismic parameters). The other families of models are built iter-
 337 atively. If the selected model does not fall into the first family, it is used as model of ref-
 338 erence to define the next family. When 24 families have been created, orphaned samples
 339 are added to the 25th family (more information in Figure S2). A second representation
 340 shows the posterior Probability Density Functions which, for a particular parameter, will
 341 inform on the amount of slip uncertainty associated to each subfault (e.g. Figures 3e-g,
 342 5c-e). Our third representation shows the median models of the 300,000 inferred samples
 343 in map view (e.g. Figures a and b in S3, S5, S9).

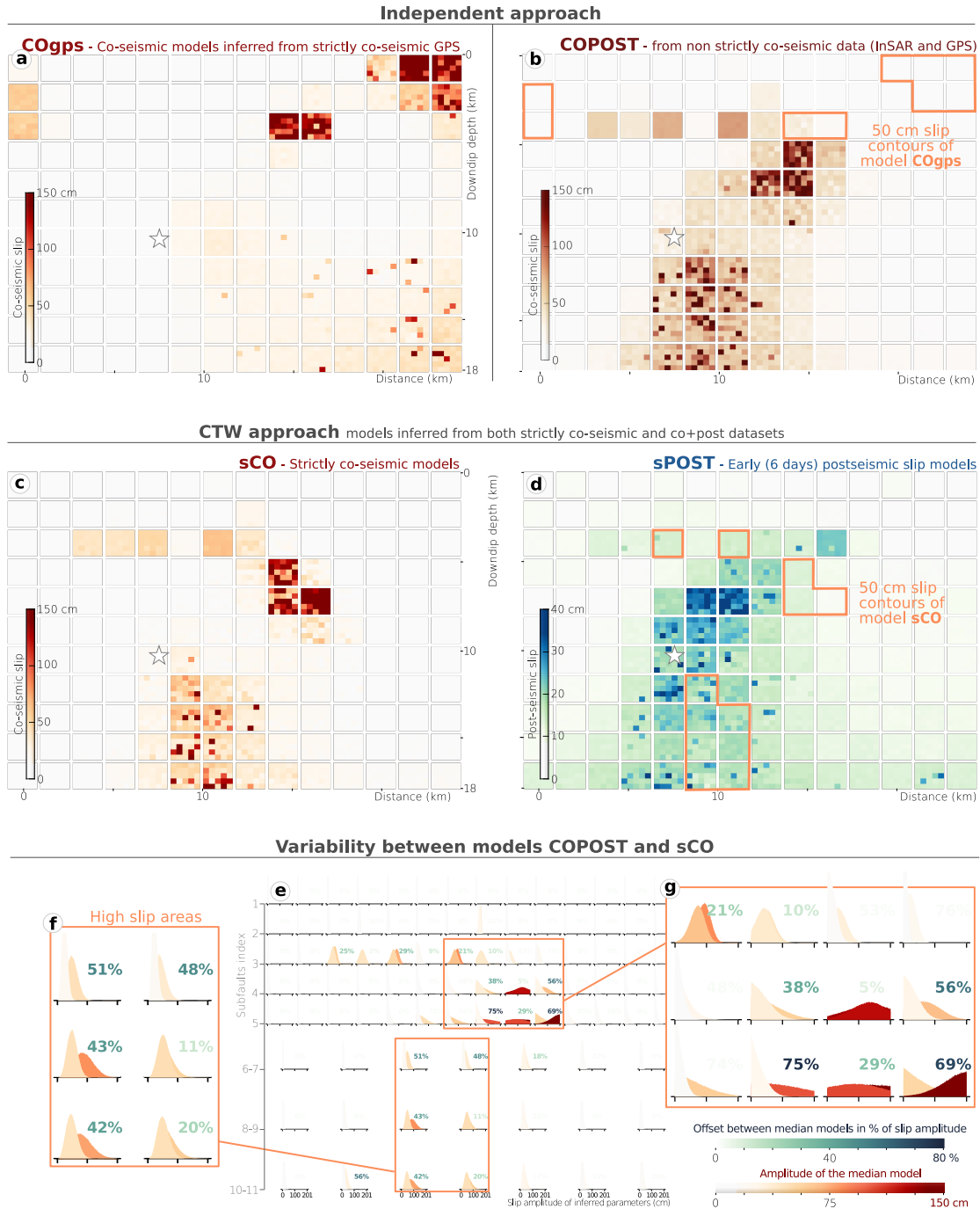


Figure 3. Comparison between finite-fault models inferred with the independent or the CTW approach. (a) Strictly co-seismic (30 s after the mainshock) slip model, named COgps, inferred from the strictly co-seismic dataset (GPS only). (b) Non-strictly co-seismic model COPOST inferred from the co-seismic dataset contaminated with some post-seismic deformation. (c) and (d) Strictly co-seismic sCO and early postseismic sPOST (6 days after the mainshock) slip models inferred jointly with the CTW approach. (a) to (d) illustrate the slip amplitude of the median models of 25 families of inferred models (more information in the text and Figure S2). Each subfault (large square) is divided into 25 pixels colored from the slip amplitude of the corresponding median model.

Figure 3. (Previous page.) (e) Comparison between the posterior Probability Density Functions of models COPOST (b) and sCO (c), colored from the amplitude of their median model. In the last four rows, the PDFs show the repartition of parameters for patches covering 2 subfaults along strike and 2 subfaults along dip (i.e. patches two times bigger than for the first four rows). The COPOST model PDFs are in the background while the sCO PDFs are in the foreground. The offset between the median models is shown as percentage with a different color scale. Two high slip areas are illustrated in detail: the highest slip patch (g) and the deep slip patch (f).

344 **4.2.1 Approaches assuming independent datasets**

345 When solving for the model COgps, we find that most of the slip is concentrated
 346 in the shallow parts of the fault (Figures 3a, S3a,c,e). Slip amplitudes reach 230 cm in
 347 the first two kilometers below the Earth surface. These values largely contradict field
 348 observations hardly reporting more than 15 cm of surface offset [*Faluccci et al.*, 2009;
 349 *Vittori et al.*, 2011]. This contradiction probably derives from our limited set of observa-
 350 tions, with only 4 GPS stations documenting the rupture in the near field (Figure 4a). The
 351 COgps model is thus largely under-determined and unlikely to represent a reliable im-
 352 age of the co-seismic deformation. In contrast, the COPOST slip model is inferred from
 353 a more populated dataset extending over a large part of the Paganica fault (Figures 3b,
 354 S3b,d,f). The patch of highest slip amplitude, reaching more than 150 cm, is well con-
 355 strained and located between 5 to 7 km depth (Figure 3b). Up to 100 cm slip is also in-
 356 ferred below the epicenter. The scalar seismic moment of model COPOST, calculated with
 357 $\mu = 3.5 \cdot 10^{10}$, is $M_0 = 4.9 \pm 0.67 \cdot 10^{25}$ dyne.m. This value corresponds to a M_w 6.4 earth-
 358 quake rather than a M_w 6.3. The comparison between observations and predicted surface
 359 displacement is shown in Figure 4 for the GPS datasets and in Figure S4 for the interfer-
 360 ograms. As expected, the COgps model well explain the "co" dataset (Figure 4b), but its
 361 predictions hardly fit the interferograms of the "co+post" dataset (Table S2). In contrast,
 362 the predicted surface displacement of the COPOST model well approaches the "co+post"
 363 observations (Figures 4b and S4), with limited residuals (Tab. S2).

364 **4.2.2 Dual time approach, without epistemic uncertainties**

365 With the CTW approach, we infer two slip models: the strictly co-seismic model
 366 sCO (see Figures 3c, S5a,c,e and S6 for an animated compilation of probable models)
 367 and the model sPOST which reflects the 6 days displacement following the mainshock
 368 (Figures 3d and S5b,d,f). The model sCO, exploiting information from both the "co" and
 369 "co+post" datasets, is in agreement with the main characteristics of the COPOST model
 370 (Figure 3b): the location and amplitude of the maximum slip patch are comparable, and
 371 a large amount of slip is also inferred at depth, up to 75 cm on average and exceeding
 372 150 cm for some models (Figure 3c). However, unlike the COPOST model, the two main
 373 slip patches of the sCO model are delimited by an unruptured area (Figure 3c). Overall,
 374 the two models differ on average by 44% and by up to 75% for some subfaults character-
 375 ized by high slip amplitudes (Figures 3e-g, S7), mainly because of the variability of the
 376 amount of slip inferred below 5 km depth. For the model sCO, $M_0 = 3.50 \pm 0.63 \cdot 10^{25}$
 377 dyne.m, corresponding to the moment magnitude value (GCMT) of 6.3.

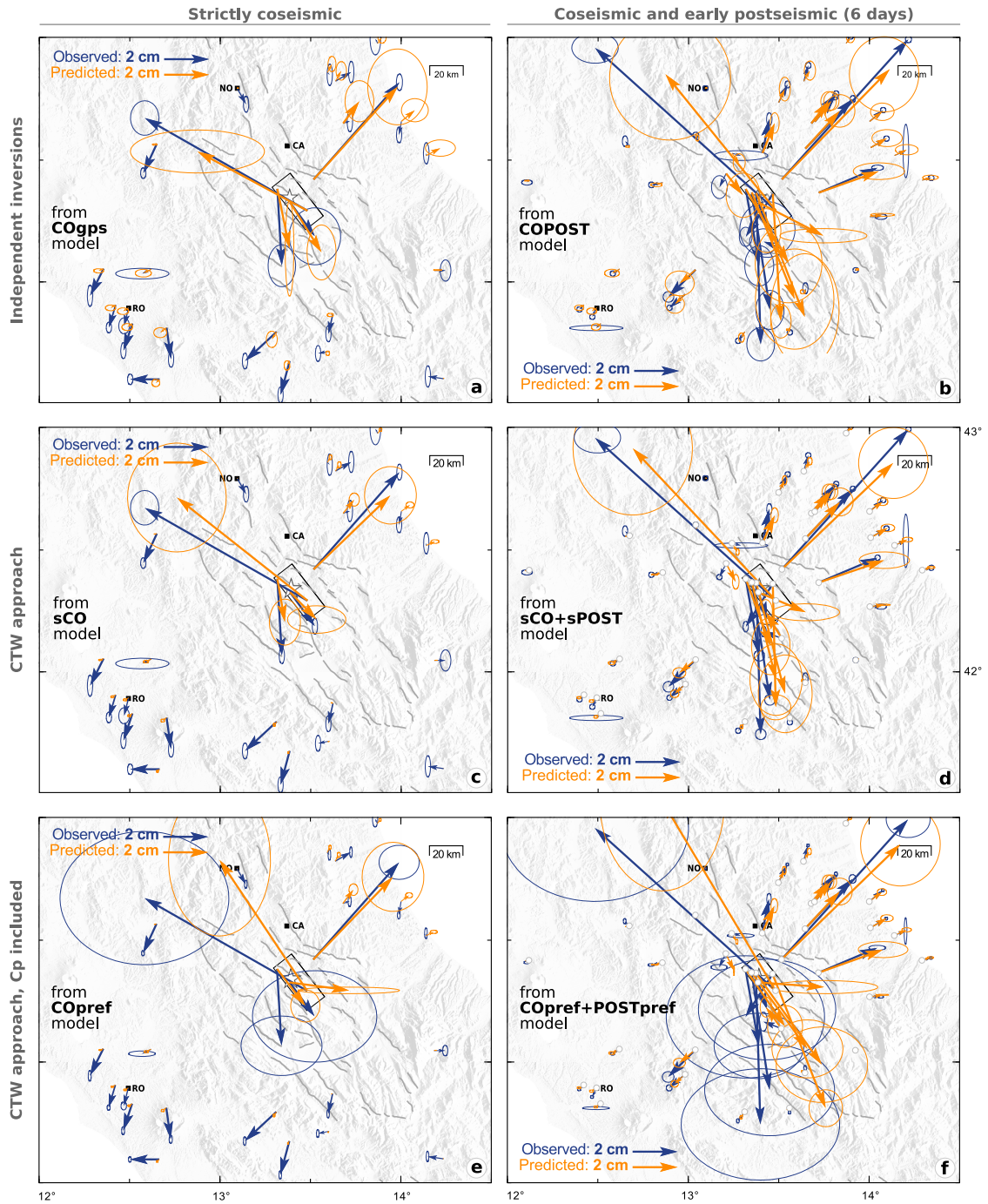


Figure 4. Comparison of horizontal surface displacement at GPS stations. Strictly co-seismic displacement is shown on the left while "co+post" displacement is shown on the right. Observed surface displacement is in blue with 95% confidence ellipses. Predictions are in orange with 95% confidence ellipses. In the top and middle rows, observational confidence ellipses (in blue) include only data errors. (a) and (b) The predictions have been calculated independently: using "co" data (a) and the "co+post" dataset (b). In (c) and (d), predictions are derived from the CTW approach. (e) and (f) show the predictions for a similar inversion setup, except epistemic uncertainties have been added to the data errors, enlarging the confidence ellipses. Our fault geometry is shown with a black rectangular box. The cities of Norcia (NO), Campotosto (CA) and Roma (RO) are indicated with black squares. Major seismogenic faults are shown in gray solid lines and the epicenter is the white star.

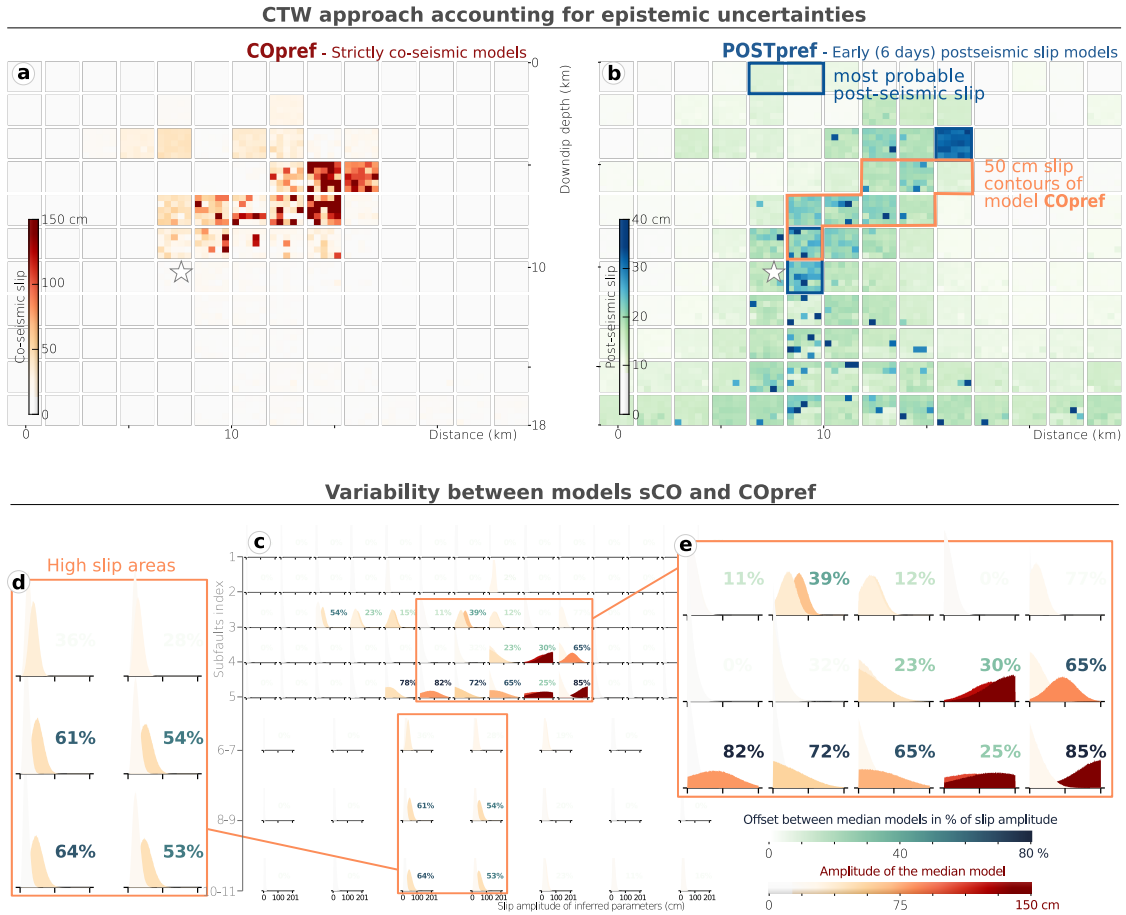


Figure 5. (a) and (b) Strictly co-seismic COpref and early postseismic POSTpref (6 days after the main-shock) preferred slip models, inferred with the CTW approach and accounting for epistemic uncertainties. (c) Comparison between the posterior Probability Density Functions of models COpref (a) and sCO (Figure 3c), colored from the amplitude of their median model. In the last four rows, the PDFs show the repartition of parameters for patches covering 2 subfaults along strike and 2 subfaults along dip (i.e. patches two times bigger than for the first four rows). The COpref model PDFs are in the foreground while the sCO PDFs are in the background. The offset between the median models is shown as percentage with a different color scale. Two high slip areas are illustrated in detail: the highest slip patch (e) and the deep slip patch (d).

378 With the CTW approach, we also find that a large portion of the fault slipped during
 379 a 6 days time window after the mainshock (Figure 3d), with maximum amplitude of
 380 30 cm in the dip-slip direction (Figure S5b). The largest post-seismic slip (> 45 cm) is
 381 located between the co-seismically ruptured patches (Figure 3c), and is well constrained
 382 with only 15 cm of posterior uncertainty (Figure S5f). Overall, post-seismic slip (30 cm
 383 and below) tends to locate around the highest co-seismic slip patch and the epicenter, but
 384 also overlaps the deepest co-seismic slip patch. Yet, below 10 km depth, the posterior un-
 385 certainty can reach 100% of the median slip amplitude, meaning that it is difficult to inter-
 386 pret anything at that level of detail (Figures S5d,f). The seismic moment of model sPOST
 387 is $M_0 = 1.58 \pm 0.63 \cdot 10^{25}$ dyne.m. The predicted surface displacements fit well the ob-
 388 servations (Figures 4c,d and Figure S8) with residuals similar to the ones of the COPOST
 389 model (Tab. S2).

390 As expected, the areas of largest post-seismic slip in the sPOST model correspond
 391 to the locations of largest divergence between COPOST and sCO models (3b-g). In sum-
 392 mary, usual approaches using independent datasets do not allow us to infer reliable im-
 393 ages of the strictly co-seismic and early post-seismic phases. Whereas the "co+post" slip
 394 model is reliable, the "co" model is not robust enough to retrieve the early afterslip from
 395 the subtraction of these two slip distributions. Additionally, the scalar seismic moment of
 396 model "co+post" corresponds to a moment magnitude greater than the GCMT M_w of 6.3.
 397 In contrast, the CTW approach allows us to infer robust estimates of both co-seismic and
 398 post-seismic slip, to exploit all the information collected within our geodetic observations,
 399 and to correctly estimate the seismic moment. However, the reliability of these models can
 400 be questioned as they do not account for uncertainties in the forward model.

401 **4.2.3 Dual time approach, accounting for epistemic uncertainties**

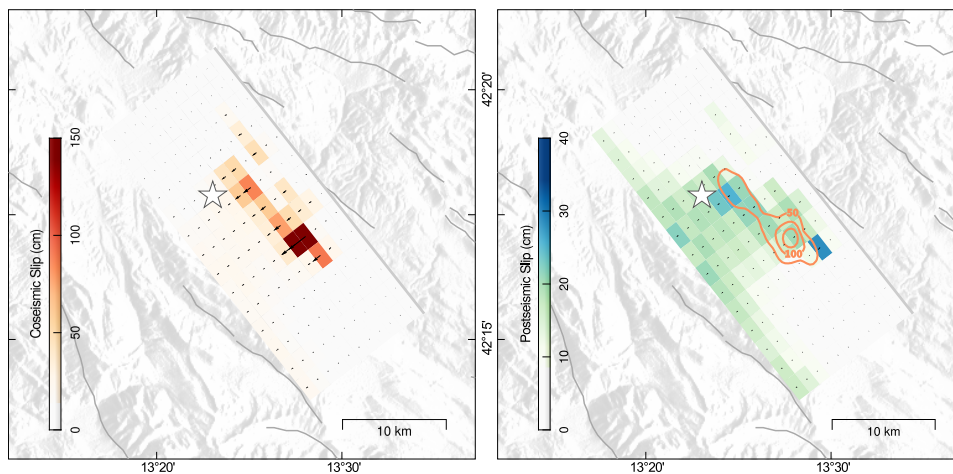


Figure 6. Our preferred slip models of the L'Aquila earthquake, inferred with the CTW approach and accounting for epistemic uncertainties. (a) and (b) show the dip-slip amplitude and rake of the average model in map view, the epicenter being the white star. In (b), orange lines also show the 50 cm co-seismic slip contours.

402 Here, we present the results of the CTW approach, as in the previous section, but
 403 accounting for epistemic uncertainties. We will name the resulting models COpref and
 404 POSTpref since they correspond to our preferred approach providing the most complete
 405 and objective evaluation of the problem (see Figures 5, 6, S9 and S11 for an animated
 406 compilation of probable co-seismic models). The distribution of the co-seismic slip differs
 407 by 42% on average and by up to 88% locally from the models inferred without accounting

408 for uncertainties (Figures 5c, S10). The co-seismic slip is now limited (on average) to a
 409 single 10 km long patch located between 5 and 10 km depth, reaching more than 150 cm
 410 amplitude to the south (right-hand side of Figure 5a). The corresponding scalar seismic
 411 moment $M_0 = 3.03 \pm 0.64 \cdot 10^{25}$ dyne.m is slightly lower than what was estimated for the
 412 model sCO but is still very close ($M_w = 6.28 \pm 0.06$) to the (GCMT) value of M_w 6.3.

413 Compared to the COpref model, the main characteristics of the POSTpref model
 414 are not strongly affected by the inclusion of uncertainties. Overall, post-seismic slip (20
 415 cm and below) occurs mostly below the co-seismic high slip patch, where almost no (less
 416 than 20 cm) co-seismic slip is imaged. Subfaults with the largest post-seismic slip (more
 417 than 40 cm) tend to be located around or on the edges of the co-seismic high slip patch
 418 (Figure 5b). The presence of large post-seismic slip below 10 km depth is unlikely as the
 419 posterior uncertainty reaches 150% of the median slip (Figure S19f). Thus, only 3 narrow
 420 zones most probably slipped post-seismically (see Figure 5b, and a comparison of median
 421 and maximum a posteriori models in Figure S12). M_0 is similar to model sPOST with a
 422 value of $1.60 \pm 0.63 \cdot 10^{25}$ dyne.m. The addition of epistemic uncertainties has increased
 423 the residuals between observations and predictions (see Tab. S2 and Figure S13). This
 424 behavior was expected as the inclusion of C_p allows the inversion to tolerate for larger
 425 misfits at data points where the forward model predictions are less reliable [Ragon *et al.*,
 426 2018].

427 In summary, the CTW approach shows that if early post-seismic is not acknowl-
 428 edged as post-seismic signal, co-seismic models may be biased by more than 40% on av-
 429 erage and of up to 75% locally. But we also learn from these different tests that adding
 430 more data into the problem is not sufficient, and epistemic uncertainties remain critical for
 431 the inference of a reliable model. Altogether, our results emphasize the need to account
 432 for two types of bias in the slip models: the contamination of co-seismic observations by
 433 some early post-seismic signal, and not acknowledging for the uncertainties associated to
 434 the forward problem.

435 5 Discussion

436 5.1 Discussion of the CTW approach

437 Observations of co-seismic or post-seismic processes are often contaminated by
 438 other sources of deformation (mainly post-seismic or co-seismic, respectively) and are
 439 widely used, when non-contaminated data are rare and scarcely distributed. Optimizing
 440 the use of the information content in each dataset is thus critical to improve the robust-
 441 ness of both co-seismic and post-seismic slip models. A first approach would be to ac-
 442 count for potential uncertainties in the co-seismic model due to early afterslip in the form
 443 of a covariance matrix, as already proposed in *Bletery et al.* [2016]. While this approach
 444 helps inferring more reliable co-seismic models at a low computational cost, it does not
 445 allow us to estimate the early afterslip and needs a prior evaluation of the amount of af-
 446 terslip considered as co-seismic signal. Another strategy would be to jointly infer "co"
 447 and "co+post" data as if they were strictly co-seismic, and to select models that better
 448 explain the "co" observations, as in [*Chlieh et al.*, 2007]. In this case, the computational
 449 cost is increased because several models have to be tested. Additionally, with these ap-
 450 proaches the early post-seismic slip is not estimated. In contrast, the CTW approach we
 451 use in this study allows us to discriminate co-seismic from early post-seismic slip and to
 452 reliably estimate corresponding slip models. Our approach takes advantage of the InSAR
 453 data that recorded both co- and post-seismic deformation to help constrain both strictly
 454 co- and early post-seismic models.

455 Our results on the L'Aquila event show that the early afterslip, here corresponding
 456 to 6 days after the co-seismic rupture, can reach a fourth to a third of the amplitude of
 457 the co-seismic slip. If the early afterslip is acknowledged as co-seismic signal, co-seismic

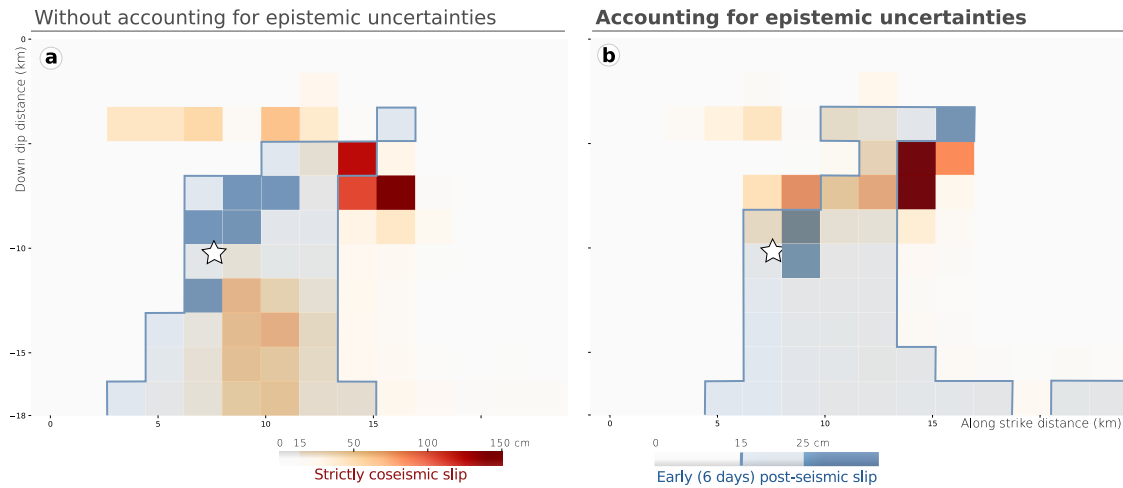


Figure 7. Effect of epistemic uncertainties (C_p) on the distribution of strictly co-seismic slip and after-slip. The slip models have been inferred accounting for epistemic uncertainties (b) or not (a). The strictly co-seismic slip median model is in light gray to dark orange colorscale. The subfaults that slipped of more than 15 to 25 cm up to 6 days after the mainshock, according to our median model, are in transparent light to medium blue. The afterslip does not overlap the co-seismic slip when C_p is accounted for (b), whereas the two slip distributions overlap at depth when no C_p is included (a).

models of the L'Aquila event are biased. The impact of early afterslip on the co-seismic models is particularly large in the case of the L'Aquila event and questions the generic nature of this result. Overall, early afterslip remains poorly studied but has been shown to range from 0.6% to more than 8% of the co-seismic peak slip in the first 3-4 hours following an earthquake [respectively for the 2009 great Tohoku-Oki earthquake and the 2012 M_w 7.6 Nicoya earthquake, *Munekane, 2012; Malservisi et al., 2015*]. Thus, that the post-seismic deformation ongoing 6 days after the mainshock reaches up to 20 % of the co-seismic slip of the L'Aquila earthquake might not be an extreme case.

Our tests also demonstrate that models are largely impacted by the introduction of epistemic uncertainties (Figure 7). This impact could mean the assumed fault and Earth properties are not realistic enough to capture the real seismic rupture, and/or that small variations of the fault geometry (slight curvature, roughness) or of the Earth model (3D heterogeneities) largely affect our slip models. The influence of epistemic uncertainties is greater on the co-seismic model, as expected from the fact that these uncertainties scale with the amount of slip [*Duputel et al., 2014; Ragon et al., 2018*]. Accounting for uncertainties of the forward model allowed us to exclude the possibility of deep slip for the co-seismic models, but not totally for the post-seismic models probably because of the much lower slip amplitudes. Additionally, accounting for C_p prevented the most probable co- and post-seismic slips to overlap in deeper parts of the fault. The inclusion of epistemic uncertainties acts like a smoothing constraint on the slip distribution, but with a smoothing factor being controlled by the inaccuracies of the forward problem.

5.2 Non-unicity of co-seismic and afterslip models of the L'Aquila earthquake

Our results on the L'Aquila event indicate that the strictly co-seismic slip is concentrated in a thin horizontal band located between 5 and 7 km depth and reaching more than 150 cm in amplitude at its southern end, with no large slip amplitudes inferred below 8 km depth (Figures 6 and 8). The highest amplitude is reached at about 6 km depth south west of the epicenter, a rupture area also imaged in the co-seismic models of *Gua-*

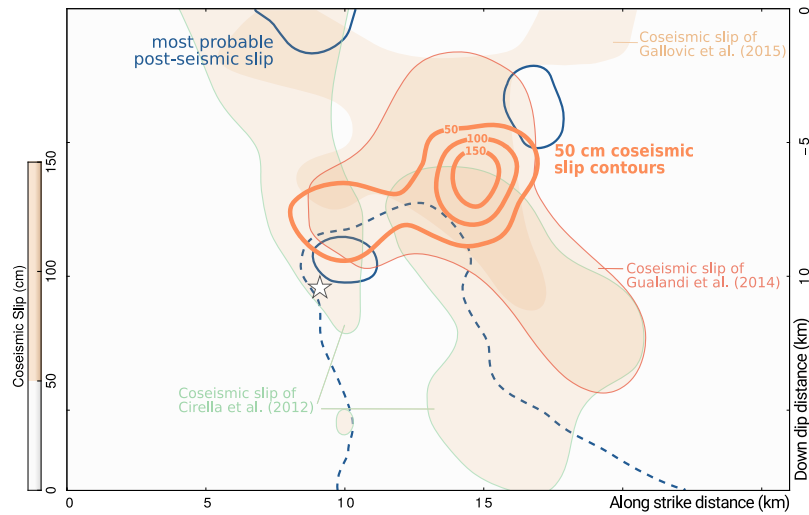


Figure 8. Comparison between the slip distributions inferred with the CTW approach and co-seismic slip distributions of other studies. The strictly co-seismic slip of *Gualandi et al.* [2014] inferred from GPS only, the strictly co-seismic slip of *Gallovic et al.* [2015] inferred from accelerometric and high rate GPS data, the co-seismic slip of *Cirella et al.* [2012] inferred from GPS, InSAR and strong motion, are projected in our fault plane in transparent light orange when slip exceeds 50 cm. The 50 cm contours of our strictly co-seismic slip distribution and the 15 cm contours of our afterslip inferred accounting for epistemic uncertainties are in bold lines, respectively orange and dark blue. The epicenter is the white star.

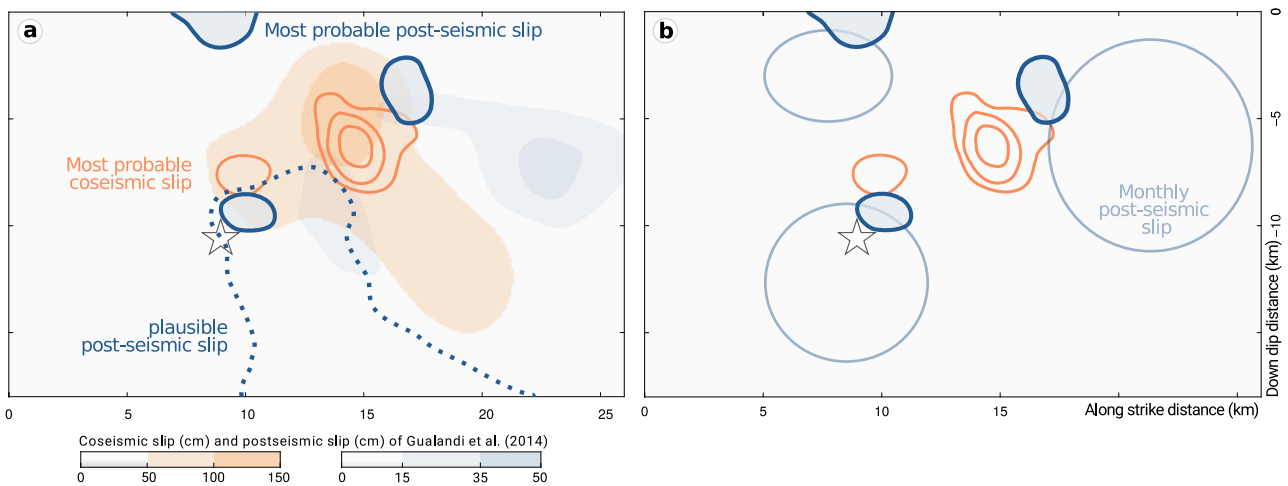


Figure 9. Comparison between our most probable strictly co- and post-seismic slip distribution 6 days after the mainshock and the post-seismic slip up to 306 days after the mainshock. (a) Our most probable slip distributions are represented with bold orange and dark blue lines, respectively for co-seismic (50 cm contours) and post-seismic slip (slip > 10 cm). The area of afterslip delimited with a dotted blue line is considered as less plausible as inferred with large uncertainties. The co-seismic slip and afterslip 306 days after the mainshock inferred by *Gualandi et al.* [2014] are plotted with the same color codes but as color swaths. (b) Our results are compared to the area that slipped post-seismically during about 6 months (176 and 194 days respectively) after the mainshock as modeled by *D'Agostino et al.* [2012] and *Cheloni et al.* [2014]. The epicenter is the white star.

485 *landi et al.* [2014], *Gallovic et al.* [2015] and *Cirella et al.* [2012] (inferred respectively
 486 from GPS only, from accelerometric and high rate GPS data, and from GPS, InSAR and
 487 strong motion, see Figure 8) and most of other authors [*Atzori et al.*, 2009; *Trasatti et al.*,
 488 2011; *D'Agostino et al.*, 2012; *Serpelloni et al.*, 2012; *Cheloni et al.*, 2014; *Balestra and*
 489 *Delouis*, 2015; *Volpe et al.*, 2015]. It is the only recurrent pattern we can notice between
 490 the 4 slip models of Figure 8. Indeed, while we do not image any shallow slip, other pub-
 491 lished slip models do with up to 1.5 m in amplitude [Figure 8, *Cirella et al.*, 2012; *Volpe*
 492 *et al.*, 2015]. At greater depths, most authors infer large slip amplitudes while our pre-
 493 ferred model shows no slip below 8 km depth.

494 The imaged patches of post-seismic slip (>15 cm) are located around our co-seismic
 495 slip, near its epicenter and southern end. Interestingly, our inferred post-seismic slip is
 496 also located near areas that ruptured co-seismically as inferred by other studies (Figure 8).
 497 The post-seismic slip that occurred several days to months after the mainshock is char-
 498 acterized by 3 wide slip areas, located SW of the main co-seismic slip patch, above the
 499 epicenter close to the surface, and around the epicenter [*D'Agostino et al.*, 2012; *Che-*
 500 *loni et al.*, 2014; *Gualandi et al.*, 2014]. Most of these post-seismic models acknowledge
 501 the first days of post-seismic signal as a co-seismic deformation. While we infer likely
 502 afterslip in similar locations, the afterslip patches are limited to narrower areas near the
 503 co-seismic rupture (Figure 9). Most of these longer-term post-seismic models cover time
 504 periods ranging from 6 days to 9 months after the mainshock, they overlook a large part
 505 of the early post-seismic deformation. Thus, the peak amplitude of the early afterslip is
 506 up to 3 times larger than what was imaged for several months by *D'Agostino et al.* [2012]
 507 and *Cheloni et al.* [2014].

508 Our results show that the amplitude and distribution of long-term afterslip may be
 509 largely underestimated (here by a factor of 3) if the deformation occurring the first few
 510 hours to days after the mainshock is not accounted in the post-seismic budget. Thus, over-
 511 looking the early part of the postseismic phase measured in geodetic data may not only
 512 bias the estimates of the coseismic slip, but also our estimates of the postseismic phase.

513 **5.3 Fault frictional properties and relationship between afterslip and aftershocks**

514 The comparison between our early post-seismic model and images of longer-term
 515 post-seismic slip suggest that afterslip may nucleate preferably around the co-seismic rup-
 516 ture in the days following the mainshock (Figure 9b). Afterwards, the afterslip propagates
 517 and extends, both along-dip and laterally, away from the co-seismic slip [*D'Agostino et al.*,
 518 2012; *Cheloni et al.*, 2014; *Gualandi et al.*, 2014]. This behavior agrees with models ex-
 519 plaining afterslip as a result of rate dependent friction behavior. Indeed, in these models
 520 the afterslip relaxes the stress increment induced in velocity-strengthening area by the
 521 co-seismic rupture [*Marone et al.*, 1991; *Perfettini and Avouac*, 2004]. The post-seismic
 522 sliding thus nucleates close to the mainshock asperity and propagates with time outward
 523 from the rupture zone. That early afterslip relates to the stress changes induced by the
 524 co-seismic rupture has also been modeled for other events [e.g. the M_w 8.0 Tokachi-oki,
 525 M_w 7.6 Chi-Chi, and the M_w 6.0 Parkfield, *Miyazaki et al.*, 2004; *Chan and Stein*, 2009;
 526 *Wang et al.*, 2012, respectively].

527 Additionally, our results show that early afterslip nucleate within narrow areas (1-2
 528 km wide), and does not happen everywhere around the co-seismic rupture. Areas sliding
 529 aseismically just after the mainshock are thus limited in size around the co-seismic rup-
 530 ture, suggesting that frictional properties vary at a small-scale around the rupture zone. It
 531 may also suggest that the regions adjacent to co-seismic rupture are potentially unstable
 532 (i.e. are steady-state velocity weakening). This interpretation agrees with the results of
 533 *Gualandi et al.* [2014] suggesting the longer-term afterslip regions, that are also located
 534 farther away from the co-seismic ruptured zone, are characterized by a transition between
 535 velocity weakening and velocity strengthening behavior. This implies that co-seismic rup-

536 ture occurs and triggers early afterslip in velocity weakening regions; while afterslip prop-
 537 agates away from the ruptured zone in fault regions that progressively become stable with
 538 the distance to the mainshock.

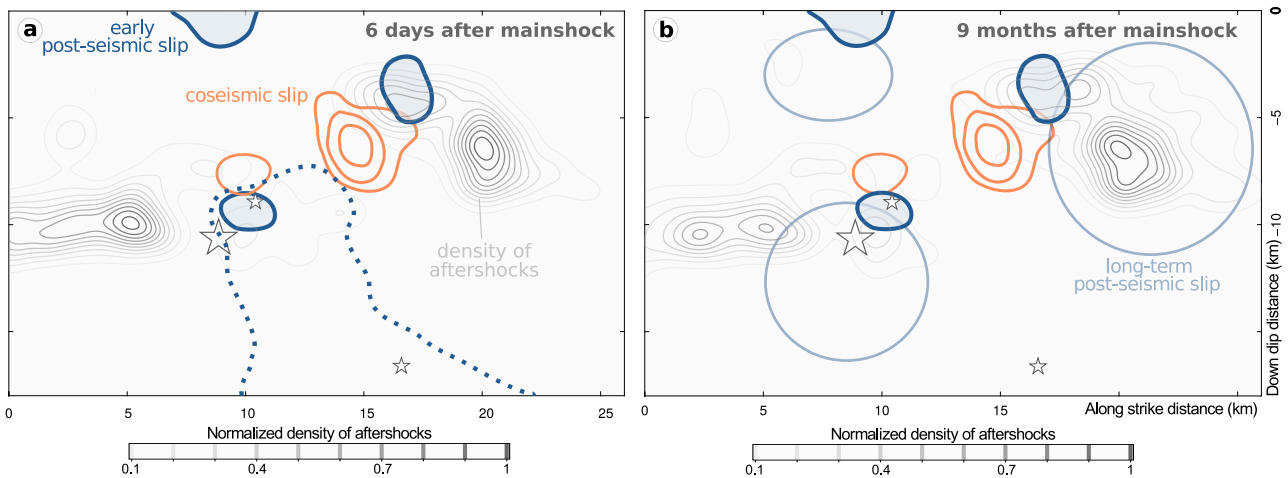


Figure 10. Distribution of most probable co-seismic slip and afterslip models, and the normalized density of aftershocks that occurred (a) within 6 days after the mainshock or (b) up to 9 months after the mainshock [$M_C = 0.88$, catalog of *Valoroso et al.*, 2013]. The strictly co-seismic 50 cm slip contours are in orange, while the contours of most probable afterslip (slip > 10 cm) are in blue. The area delimited by dotted blue lines has plausibly hosted some afterslip, but not as probably as the other regions. The areas that slipped post-seismically during about 6 months after the mainshock as modeled by *D’Agostino et al.* [2012], *Cheloni et al.* [2014] and *Gualandi et al.* [2014] are the blue circles. The density of aftershocks located within 3 km of the fault (to account for potential uncertainty of the fault geometry) is calculated with a kernel density estimation method [*Parzen*, 1962] with a smoothing factor of 0.6. The cumulated number of aftershocks of $M_C = 0.88$ is of ~ 6000 6 days after the mainshock and 8 times larger 9 months after the mainshock (Figure S14). The epicenter and aftershocks of $M_w \geq 4.4$ are the white stars.

539 In Figure 10, we compare the slip distributions imaged for the mainshock and 6
 540 days after, with the distribution of aftershocks detected over 6 days and 9 months after the
 541 mainshock [*Valoroso et al.*, 2013]. As for many earthquakes, aftershocks are distributed
 542 mainly at the ends of the fault [*Das and Henry*, 2003] with few events located near the
 543 co-seismic rupture. Six days after the mainshock (Figure 10a), our results show no clear
 544 correlation between the location of early afterslip and aftershocks. Months after the main-
 545 shock, the areas with a high density of aftershocks are similar to 6 days after the main-
 546 shock [as suggested by *Henry and Das*, 2001, whereas the cumulated number of after-
 547 shocks is 8 times larger, see Figure S14] and the post-seismic slip has extended farther
 548 away from the co-seismic rupture. This is why we can observe a spatial correlation be-
 549 tween some areas of long-term post-seismic slip and aftershocks [*D’Agostino et al.*, 2012;
 550 *Cheloni et al.*, 2014]. The spatial correlation is particularly striking for the southern after-
 551 afterslip patch, for which few early aftershocks are located within the early afterslip area
 552 (Figure 10a) while the aftershock cluster overlies the monthly afterslip that propagated
 553 outward from the co-seismically ruptured zone (Figure 10b).

554 From our results, we can thus draw only one conclusion: there is no correlation be-
 555 tween the area of large (>15 cm) early afterslip and the location of aftershocks for the
 556 first few days after the mainshock. This conclusion contradicts the observations made for
 557 some other earthquakes although mainly at longer time scales [e.g. *Hsu et al.*, 2006; *Per-
 558 fettini and Avouac*, 2007; *Wang et al.*, 2012; *Ross et al.*, 2017, for time periods spanning

559 respectively 11 months, 3.5 years, 5 days and 2.5 months]. Our results could also suggest
 560 that, for some parts of the fault, aftershocks nucleation precedes aseismic slip that occur
 561 months after the mainshock; aftershocks could thus be partly explained by stress changes
 562 due to the co-seismic rupture. But these aftershocks could also be triggered by early af-
 563 terslip with an amplitude so low that it is not inferred by our model. The absence of clear
 564 correlation between early afterslip and aftershocks may also be related to the presence of
 565 high pressure fluids in the seismogenic zone of the L'Aquila event, and of Central Italy
 566 in general, with the widespread emissions of CO₂ rich fluids for deep origin [*Chiodini*
 567 *et al.*, 2000; *Frezzotti et al.*, 2009; *Chiodini et al.*, 2011]. Already, *Miller et al.* [2004] and
 568 *Antonoli et al.* [2005] proposed that the aftershocks and spatio-temporal migration of
 569 the seismicity of the 1997 Umbria-Marche seismic sequence (80 km NE of the L'Aquila
 570 event) were driven by the co-seismically induced fluid pressure migration. Similarly, the
 571 increase in seismicity rate of the L'Aquila earthquake and the occurrence of some after-
 572 shocks may have been driven by fluid flows [*Luccio et al.*, 2010; *Terakawa et al.*, 2010;
 573 *Malagnini et al.*, 2012]. High pressure fluids have been observed before the co-seismic
 574 rupture, and may have impacted the nucleation phase of the L'Aquila earthquake [*Lucente*
 575 *et al.*, 2010]. Finally, *Malagnini et al.* [2012] show that the strength of the Campotosto
 576 fault, just north of the main rupture (see Figure 2), has been controlled by fluid migration
 577 for at least 6 days after the mainshock, a time window corresponding to our study of early
 578 afterslip. The perturbations in pore fluid pressure induced by the co-seismic rupture may
 579 have triggered the first aftershocks of the L'Aquila earthquake. Fluid migration may have
 580 prevented aftershocks and early afterslip to affect the same areas of the fault, especially if
 581 the increase in fluid pressure first produced aseismic slip, followed by triggered seismicity
 582 around the pore pressure front [*Miller et al.*, 2004]. Finally, if early aftershocks were trig-
 583 gered by changes in fluid pressure, it may justify the possibility that some of these early
 584 aftershocks nucleated before the occurrence of long-term afterslip in similar regions of the
 585 fault.

586 6 Conclusion

587 In this study, we use a simple and efficient approach to account for the differences
 588 in temporal resolution of various geodetic datasets. A redesign of the Green's Functions
 589 matrix allows us to optimize the use of the information content of datasets covering differ-
 590 ent time periods. With this approach, we image simultaneously the strictly co-seismic slip
 591 and the early afterslip (6 days after the mainshock) of the 2009 M_w6.3 L'Aquila earth-
 592 quake using two datasets: one covers the two slip episodes (e.g. InSAR) while the other
 593 records the co-seismic signal only (e.g. continuous GNSS). We show that when the two
 594 phases are inverted independently, as is usually the case, the estimated slip distributions
 595 are not reliable because strictly co-seismic observations are usually of poor spatial reso-
 596 lution. Additionally, overlooking the early post-seismic deformation results in models that
 597 overestimates the co-seismic slip, and underestimates the total post-seismic slip budget.
 598 In contrast, our approach allows us to accurately estimate both co-seismic and early post-
 599 seismic slip models.

600 Our results show that neglecting the contribution of the early post-seismic defor-
 601 mation will likely bias estimates of the co-seismic and/or the post-seismic slip. For our
 602 test case of the L'Aquila earthquake, the peak co-seismic slip is likely 30% greater when
 603 early post-seismic signal is recorded as co-seismic deformation. The long-term afterslip
 604 estimates are underestimated by a factor 3 when the first 6 days of post-seismic defor-
 605 mation are not acknowledged. Our investigation of the L'Aquila event also stressed the
 606 strong influence of uncertainties in the forward model, mainly stemming from our imper-
 607 fect knowledge of the fault geometry and the Earth structure, on the imaged slip distribu-
 608 tions. These uncertainties alone are sufficient to cause contradictory interpretations on the
 609 slip history on the fault (e.g. with the existence of shallow or dip slip).

610 Our preferred slip model for the L'Aquila earthquake tends to be simpler than many
 611 previous models, with one thin horizontal band of slip located around 7km depth, reach-
 612 ing 150cm in amplitude near its southern end. Our model thus excludes the possibility
 613 of major shallow or deep co-seismic slip patches (less than a few km or deeper than 10).
 614 The early post-seismic slip (6 days after the mainshock) was limited to the same inter-
 615 mediate depth range (7 km +/- 3 km), initiating on the edges of the co-seismic slip, with
 616 possibly some overlap. Some afterslip may also have occurred at greater depths. A com-
 617 parison with longer term afterslip models suggest that the early afterslip patches might
 618 have simply expanded over time from their initial position. Aftershocks are more spatially
 619 distributed (7 km +/- 5 km) but still concentrated at intermediate depth. Several studies
 620 suggest that aftershocks might be driven by afterslip [e.g., *Perfettini and Avouac*, 2007;
 621 *Hsu et al.*, 2006; *Sladen et al.*, 2010; *Ross et al.*, 2017; *Perfettini et al.*, 2018] but here af-
 622 tershocks are only partially overlapping. This result suggests that post-seismic reloading
 623 may be influenced by fluids as advocated in several previous studies [e.g., *Luccio et al.*,
 624 2010; *Terakawa et al.*, 2010; *Malagnini et al.*, 2012; *Guglielmi et al.*, 2015; *Scuderi and*
 625 *Collettini*, 2016].

626 Acknowledgments

627 We thank Bertrand Delouis and Frederic Cappa for helpful discussions. We are extremely
 628 grateful to Federica Magnoni who shared her 3D crustal model for the L'Aquila area
 629 [*Magnoni et al.*, 2014], to Luisa Valoroso who provided the aftershock catalog for the
 630 L'Aquila earthquake [*Valoroso et al.*, 2013] and to Simone Atzori for sharing the InSAR
 631 data [*Atzori et al.*, 2009]. The Bayesian simulations were performed on the HPC-Regional
 632 Center ROMEO (<https://romeo.univ-reims.fr>) of the University of Reims Champagne-
 633 Ardenne (France). The Classic Slip Inversion (CSI) Python library created by Romain Jo-
 634 livet was used to build inputs for the Bayesian algorithm. Discussed slip models of *Gua-*
 635 *landi et al.* [2014], *Gallovic et al.* [2015] and *Cirella et al.* [2012] have been retrieved from
 636 SRCMOD [<http://equake-rc.info/SRCMOD/>], *Mai and Thingbaijam*, 2014]. Figures were
 637 generated with the Matplotlib and Seaborn Python libraries and with the Generic Mapping
 638 Tools library. This study was partly supported by the French National Research Agency
 639 (ANR) EPOST project ANR-14-CE03-0002. Théa Ragon is supported by a fellowship
 640 from the French Ministry of Research and Higher Education.

641 References

- 642 Albano, M., S. Barba, M. Saroli, M. Moro, F. Malvarosa, M. Costantini, C. Bignami, and
 643 S. Stramondo (2015), Gravity-driven postseismic deformation following the Mw 6.3
 644 2009 L'Aquila (Italy) earthquake, *Scientific Reports*, 5, doi:10.1038/srep16558.
- 645 Antonioli, A., D. Piccinini, L. Chiaraluce, and M. Cocco (2005), Fluid flow and seismic-
 646 ity pattern: Evidence from the 1997 Umbria-Marche (central Italy) seismic sequence,
 647 *Geophysical Research Letters*, 32(10), doi:10.1029/2004GL022256.
- 648 Anzidei, M., E. Boschi, V. Cannelli, R. Devoti, A. Esposito, A. Galvani, D. Melini,
 649 G. Pietrantonio, F. Riguzzi, V. Sepe, and E. Serpelloni (2009), Coseismic deformation
 650 of the destructive April 6, 2009 L'Aquila earthquake (central Italy) from GPS data,
 651 *Geophysical Research Letters*, 36(17), L17,307, doi:10.1029/2009GL039145.
- 652 Atzori, S., I. Hunstad, M. Chini, S. Salvi, C. Tolomei, C. Bignami, S. Stramondo,
 653 E. Trasatti, A. Antonioli, and E. Boschi (2009), Finite fault inversion of DInSAR co-
 654 seismic displacement of the 2009 L'Aquila earthquake (central Italy), *Geophysical Re-*
 655 *search Letters*, 36(15), L15,305, doi:10.1029/2009GL039293.
- 656 Avallone, A., M. Marzario, A. Cirella, A. Piatanesi, A. Rovelli, C. Di Alessandro,
 657 E. D'Anastasio, N. D'Agostino, R. Giuliani, and M. Mattone (2011), Very high rate
 658 (10 Hz) GPS seismology for moderate-magnitude earthquakes: The case of the Mw 6.3
 659 L'Aquila (central Italy) event, *Journal of Geophysical Research: Solid Earth*, 116(B2),
 660 B02,305, doi:10.1029/2010JB007834.

- 661 Balestra, J., and B. Delouis (2015), Reassessing the Rupture Process of the 2009 L'Aquila
662 Earthquake (Mw 6.3) on the Paganica Fault and Investigating the Possibility of Co-
663 seismic Motion on Secondary Faults, *Bulletin of the Seismological Society of America*,
664 *105*(3), 1517–1539, doi:10.1785/0120140239.
- 665 Barbot, S., and Y. Fialko (2010), A unified continuum representation of post-seismic re-
666 laxation mechanisms: semi-analytic models of afterslip, poroelastic rebound and vis-
667 coelastic flow, *Geophysical Journal International*, *182*(3), 1124–1140, doi:10.1111/j.
668 1365-246X.2010.04678.x.
- 669 Barnhart, W. D., C. M. J. Brengman, S. Li, and K. E. Peterson (2018), Ramp-flat base-
670 ment structures of the Zagros Mountains inferred from co-seismic slip and afterslip of
671 the 2017 Mw7.3 Darbandikhan, Iran/Iraq earthquake, *Earth and Planetary Science Let-
672 ters*, *496*, 96–107, doi:10.1016/j.epsl.2018.05.036.
- 673 Bletery, Q., A. Sladen, J. Jiang, and M. Simons (2016), A Bayesian source model for the
674 2004 great Sumatra-Andaman earthquake, *Journal of Geophysical Research: Solid Earth*,
675 p. 2016JB012911, doi:10.1002/2016JB012911.
- 676 Boncio, P., G. Lavecchia, G. Milana, and B. Rozzi (2004a), Seismogenesis in Central
677 Apennines, Italy: an integrated analysis of minor earthquake sequences and structural
678 data in the Amatrice-Campotosto area, *Annals of Geophysics*, *47*(6), 1723–1742.
- 679 Boncio, P., G. Lavecchia, and B. Pace (2004b), Defining a model of 3d seismogenic
680 sources for Seismic Hazard Assessment applications: The case of central Apennines
681 (Italy), *Journal of Seismology*, *8*(3), 407–425, doi:10.1023/B:JOSE.0000038449.78801.
682 05.
- 683 Boncio, P., A. Pizzi, F. Brozzetti, G. Pomposo, G. Lavecchia, D. Di Naccio, and F. Fer-
684 rarini (2010), Coseismic ground deformation of the 6 April 2009 L'Aquila earth-
685 quake (central Italy, Mw6.3), *Geophysical Research Letters*, *37*(6), L06,308, doi:
686 10.1029/2010GL042807.
- 687 Burgmann, R., P. Segall, M. Lisowski, and J. Svarc (1997), Postseismic strain following
688 the 1989 Loma Prieta earthquake from GPS and leveling measurements, *Journal of Geo-
689 physical Research: Solid Earth*, *102*(B3), 4933–4955, doi:10.1029/96JB03171.
- 690 Chan, C.-H., and R. S. Stein (2009), Stress evolution following the 1999 Chi-Chi, Tai-
691 wan, earthquake: Consequences for afterslip, relaxation, aftershocks and departures
692 from Omori decay, *Geophysical Journal International*, *177*(1), 179–192, doi:10.1111/
693 j.1365-246X.2008.04069.x.
- 694 Cheloni, D., N. D'Agostino, E. D'Anastasio, A. Avallone, S. Mantenuto, R. Giuliani,
695 M. Mattone, S. Calcaterra, P. Gambino, D. Dominici, F. Radicioni, and G. Fastellini
696 (2010), Coseismic and initial post-seismic slip of the 2009 Mw 6.3 L'Aquila earth-
697 quake, Italy, from GPS measurements, *Geophysical Journal International*, *181*(3),
698 1539–1546, doi:10.1111/j.1365-246X.2010.04584.x.
- 699 Cheloni, D., R. Giuliani, E. D'Anastasio, S. Atzori, R. J. Walters, L. Bonci,
700 N. D'Agostino, M. Mattone, S. Calcaterra, P. Gambino, F. Deninno, R. Maseroli, and
701 G. Stefanelli (2014), Coseismic and post-seismic slip of the 2009 L'Aquila (central
702 Italy) MW 6.3 earthquake and implications for seismic potential along the Campotosto
703 fault from joint inversion of high-precision levelling, InSAR and GPS data, *Tectono-
704 physics*, *622*, 168–185, doi:10.1016/j.tecto.2014.03.009.
- 705 Chiarabba, C., A. Amato, M. Anselmi, P. Baccheschi, I. Bianchi, M. Cattaneo, G. Ce-
706 cere, L. Chiaraluca, M. G. Ciaccio, P. De Gori, G. De Luca, M. Di Bona, R. Di Ste-
707 fano, L. Faenza, A. Govoni, L. Improta, F. P. Lucente, A. Marchetti, L. Margheriti,
708 F. Mele, A. Michelini, G. Monachesi, M. Moretti, M. Pastori, N. Piana Agostinetti,
709 D. Piccinini, P. Roselli, D. Seccia, and L. Valoroso (2009), The 2009 L'Aquila (central
710 Italy) MW6.3 earthquake: Main shock and aftershocks, *Geophysical Research Letters*,
711 *36*(18), L18,308, doi:10.1029/2009GL039627.
- 712 Chiaraluca, L. (2012), Unravelling the complexity of Apenninic extensional fault systems:
713 A review of the 2009 L'Aquila earthquake (Central Apennines, Italy), *Journal of Struc-
714 tural Geology*, *42*, 2–18, doi:10.1016/j.jsg.2012.06.007.

- 715 Chiaraluce, L., L. Valoroso, D. Piccinini, R. Di Stefano, and P. De Gori (2011), The
 716 anatomy of the 2009 L'Aquila normal fault system (central Italy) imaged by high reso-
 717 lution foreshock and aftershock locations, *Journal of Geophysical Research: Solid Earth*,
 718 *116*(B12), B12,311, doi:10.1029/2011JB008352.
- 719 Chiodini, G., F. Frondini, C. Cardellini, F. Parello, and L. Peruzzi (2000), Rate of diffuse
 720 carbon dioxide Earth degassing estimated from carbon balance of regional aquifers: The
 721 case of central Apennine, Italy, *Journal of Geophysical Research: Solid Earth*, *105*(B4),
 722 8423–8434, doi:10.1029/1999JB900355.
- 723 Chiodini, G., S. Caliro, C. Cardellini, F. Frondini, S. Inguaggiato, and F. Matteucci
 724 (2011), Geochemical evidence for and characterization of CO₂ rich gas sources in the
 725 epicentral area of the Abruzzo 2009 earthquakes, *Earth and Planetary Science Letters*,
 726 *304*(3), 389–398, doi:10.1016/j.epsl.2011.02.016.
- 727 Chlieh, M., J.-P. Avouac, V. Hjorleifsdottir, T.-R. A. Song, C. Ji, K. Sieh, A. Sladen,
 728 H. Hebert, L. Prawirodirdjo, Y. Bock, and J. Galetzka (2007), Coseismic Slip and Af-
 729 terslip of the Great Mw 9.15 Sumatra-Andaman Earthquake of 2004, *Bulletin of the Seis-
 730 mological Society of America*, *97*(1A), S152–S173, doi:10.1785/0120050631.
- 731 Cirella, A., A. Piatanesi, E. Tinti, M. Chini, and M. Cocco (2012), Complexity of the rup-
 732 ture process during the 2009 L'Aquila, Italy, earthquake, *Geophysical Journal Interna-
 733 tional*, *190*(1), 607–621, doi:10.1111/j.1365-246X.2012.05505.x.
- 734 Cubas, N., N. Lapusta, J.-P. Avouac, and H. Perfettini (2015), Numerical modeling of
 735 long-term earthquake sequences on the NE Japan megathrust: Comparison with ob-
 736 servations and implications for fault friction, *Earth and Planetary Science Letters*,
 737 *419*(Supplement C), 187–198, doi:10.1016/j.epsl.2015.03.002.
- 738 D'Agostino, N., D. Cheloni, G. Fornaro, R. Giuliani, and D. Reale (2012), Space-time
 739 distribution of afterslip following the 2009 L'Aquila earthquake, *Journal of Geophysical
 740 Research: Solid Earth*, *117*(B2), B02,402, doi:10.1029/2011JB008523.
- 741 Das, S., and C. Henry (2003), Spatial relation between main earthquake slip and its after-
 742 shock distribution, *Reviews of Geophysics*, *41*(3), doi:10.1029/2002RG000119.
- 743 Delouis, B., D. Giardini, P. Lundgren, and J. Salichon (2002), Joint Inversion of InSAR,
 744 GPS, Teleseismic, and Strong-Motion Data for the Spatial and Temporal Distribution of
 745 Earthquake Slip: Application to the 1999 izmit Mainshock, *Bulletin of the Seismological
 746 Society of America*, *92*(1), 278–299, doi:10.1785/0120000806.
- 747 Dieterich, J. (1994), A constitutive law for rate of earthquake production and its appli-
 748 cation to earthquake clustering, *Journal of Geophysical Research: Solid Earth*, *99*(B2),
 749 2601–2618, doi:10.1029/93JB02581.
- 750 Duputel, Z., P. S. Agram, M. Simons, S. E. Minson, and J. L. Beck (2014), Accounting
 751 for prediction uncertainty when inferring subsurface fault slip, *Geophysical journal in-
 752 ternational*, *197*(1), 464–482.
- 753 Elliott, J. R., A. C. Copley, R. Holley, K. Scharer, and B. Parsons (2013), The 2011 Mw
 754 7.1 Van (Eastern Turkey) earthquake, *Journal of Geophysical Research: Solid Earth*,
 755 *118*(4), 1619–1637, doi:10.1002/jgrb.50117.
- 756 EMERGE Working Group (2010), Evidence for surface rupture associated with the
 757 Mw 6.3 L'Aquila earthquake sequence of April 2009 (central Italy), *Terra Nova*, *22*(1),
 758 43–51, doi:10.1111/j.1365-3121.2009.00915.x.
- 759 Falcucci, E., S. Gori, E. Peronace, G. Fubelli, M. Moro, M. Saroli, B. Giaccio,
 760 P. Messina, G. Naso, G. Scardia, A. Sposato, M. Voltaggio, P. Galli, and F. Galadini
 761 (2009), The Paganica Fault and Surface Coseismic Ruptures Caused by the 6 April
 762 2009 Earthquake (L'Aquila, Central Italy), *Seismological Research Letters*, *80*(6),
 763 940–950, doi:10.1785/gssrl.80.6.940.
- 764 Freed, A. M. (2007), Afterslip (and only afterslip) following the 2004 Parkfield, Cal-
 765 ifornia, earthquake, *Geophysical Research Letters*, *34*(6), L06,312, doi:10.1029/
 766 2006GL029155.
- 767 Freed, A. M., and R. Burgmann (2004), Evidence of power-law flow in the Mojave desert
 768 mantle, *Nature*, *430*(6999), 548–51.

- 769 Frezzotti, M. L., A. Peccerillo, and G. Panza (2009), Carbonate metasomatism and CO₂
770 lithosphereasthenosphere degassing beneath the Western Mediterranean: An integrated
771 model arising from petrological and geophysical data, *Chemical Geology*, 262(1),
772 108–120, doi:10.1016/j.chemgeo.2009.02.015.
- 773 Gallovic, F., W. Imperatori, and P. M. Mai (2015), Effects of three-dimensional crustal
774 structure and smoothing constraint on earthquake slip inversions: Case study of the
775 Mw6.3 2009 L'Aquila earthquake, *Journal of Geophysical Research: Solid Earth*,
776 120(1), 2014JB011,650, doi:10.1002/2014JB011650.
- 777 Gualandi, A., E. Serpelloni, and M. E. Belardinelli (2014), Space-time evolution of crustal
778 deformation related to the Mw 6.3, 2009 L'Aquila earthquake (central Italy) from prin-
779 cipal component analysis inversion of GPS position time-series, *Geophysical Journal*
780 *International*, p. ggt522, doi:10.1093/gji/ggt522.
- 781 Gualandi, A., J.-P. Avouac, J. Galetzka, J. F. Genrich, G. Blewitt, L. B. Adhikari, B. P.
782 Koirala, R. Gupta, B. N. Upreti, B. Pratt-Sitaula, and J. Liu-Zeng (2017), Pre- and post-
783 seismic deformation related to the 2015, Mw7.8 Gorkha earthquake, Nepal, *Tectono-*
784 *physics*, 714(Supplement C), 90–106, doi:10.1016/j.tecto.2016.06.014.
- 785 Guglielmi, Y., F. Cappa, J.-P. Avouac, P. Henry, and D. Elsworth (2015), Seismicity trig-
786 gered by fluid injectioninduced aseismic slip, *Science*, 348(6240), 1224–1226, doi:
787 10.1126/science.aab0476.
- 788 He, P., E. A. Hetland, Q. Wang, K. Ding, Y. Wen, and R. Zou (2017), Coseismic Slip in
789 the 2016 Mw 7.8 Ecuador Earthquake Imaged from Sentinel-1a Radar Interferometry,
790 *Seismological Research Letters*, 88(2A), 277–286, doi:10.1785/0220160151.
- 791 Helmstetter, A., and B. E. Shaw (2009), Afterslip and aftershocks in the rate-and-state
792 friction law, *Journal of Geophysical Research: Solid Earth*, 114(B1), doi:10.1029/
793 2007JB005077.
- 794 Henry, C., and S. Das (2001), Aftershock zones of large shallow earthquakes: fault di-
795 mensions, aftershock area expansion and scaling relations, *Geophysical Journal Interna-*
796 *tional*, 147(2), 272–293, doi:10.1046/j.1365-246X.2001.00522.x.
- 797 Herrmann, R. B., L. Malagnini, and I. Munafo (2011), Regional Moment Tensors of the
798 2009 L'Aquila Earthquake Sequence, *Bulletin of the Seismological Society of America*,
799 101(3), 975–993, doi:10.1785/0120100184.
- 800 Hsu, Y.-J., M. Simons, J.-P. Avouac, J. Galetzka, K. Sieh, M. Chlieh, D. Natawidjaja,
801 L. Prawirodirdjo, and Y. Bock (2006), Frictional Afterslip Following the 2005 Nias-
802 Simeulue Earthquake, Sumatra, *Science*, 312(5782), 1921–1926, doi:10.1126/science.
803 1126960.
- 804 Johnson, K. M., J. Fukuda, and P. Segall (2012), Challenging the rate-state asperity
805 model: Afterslip following the 2011 M9 Tohoku-oki, Japan, earthquake, *Geophysical*
806 *Research Letters*, 39(20), L20,302, doi:10.1029/2012GL052901.
- 807 Jonsson, S., P. Segall, R. Pedersen, and G. Bjornsson (2003), Post-earthquake ground
808 movements correlated to pore-pressure transients, *Nature*, 424(6945), 179–83.
- 809 Jolivet, R., C. Lasserre, M.-P. Doin, S. Guillaso, G. Peltzer, R. Dailu, J. Sun, Z.-K. Shen,
810 and X. Xu (2012), Shallow creep on the Haiyuan Fault (Gansu, China) revealed by
811 SAR Interferometry, *Journal of Geophysical Research: Solid Earth*, 117(B6), B06,401,
812 doi:10.1029/2011JB008732.
- 813 Lavecchia, G., F. Ferrarini, F. Brozzetti, R. D. Nardis, P. Boncio, and L. Chiaraluce
814 (2012), From surface geology to aftershock analysis: Constraints on the geometry of
815 the L'Aquila 2009 seismogenic fault system, *Italian Journal of Geosciences*, 131(3),
816 330–347, doi:10.3301/IJG.2012.24.
- 817 Lin, Y.-n. N., A. Sladen, F. Ortega-Culaciati, M. Simons, J.-P. Avouac, E. J. Fielding,
818 B. A. Brooks, M. Bevis, J. Genrich, A. Rietbrock, C. Vigny, R. Smalley, and A. Soc-
819 quet (2013), Coseismic and postseismic slip associated with the 2010 Maule Earth-
820 quake, Chile: Characterizing the Arauco Peninsula barrier effect, *Journal of Geophysical*
821 *Research: Solid Earth*, 118(6), 3142–3159, doi:10.1002/jgrb.50207.

- 822 Lohman, R. B., and M. Simons (2005), Some thoughts on the use of InSAR data to con-
823 strain models of surface deformation: Noise structure and data downsampling, *Geo-*
824 *chemistry, Geophysics, Geosystems*, 6(1), Q01,007, doi:10.1029/2004GC000841.
- 825 Luccio, F. D., G. Ventura, R. D. Giovambattista, A. Piscini, and F. R. Cinti (2010), Nor-
826 mal faults and thrusts reactivated by deep fluids: The 6 April 2009 Mw 6.3 L'Aquila
827 earthquake, central Italy, *Journal of Geophysical Research: Solid Earth*, 115(B6), doi:
828 10.1029/2009JB007190.
- 829 Lucente, F. P., P. D. Gori, L. Margheriti, D. Piccinini, M. D. Bona, C. Chiarabba, and
830 N. P. Agostinetti (2010), Temporal variation of seismic velocity and anisotropy be-
831 fore the 2009 MW 6.3 L'Aquila earthquake, Italy, *Geology*, 38(11), 1015–1018, doi:
832 10.1130/G31463.1.
- 833 Magnoni, F., E. Casarotti, A. Michelini, A. Piersanti, D. Komatitsch, D. Peter, and
834 J. Tromp (2014), Spectral Element Simulations of Seismic Waves Generated by the
835 2009 L'Aquila Earthquake, *Bulletin of the Seismological Society of America*, 104(1),
836 73–94, doi:10.1785/0120130106.
- 837 Mai, P. M., and K. K. S. Thingbaijam (2014), SRCMOD: An Online Database of Finite-
838 Fault Rupture Models, *Seismological Research Letters*, 85(6), 1348–1357, doi:10.1785/
839 0220140077.
- 840 Malagnini, L., F. P. Lucente, P. D. Gori, A. Akinci, and I. Munafo' (2012), Control of
841 pore fluid pressure diffusion on fault failure mode: Insights from the 2009 L'Aquila
842 seismic sequence, *Journal of Geophysical Research: Solid Earth*, 117(B5), doi:10.1029/
843 2011JB008911.
- 844 Malservisi, R., S. Y. Schwartz, N. Voss, M. Protti, V. Gonzalez, T. H. Dixon, Y. Jiang,
845 A. V. Newman, J. Richardson, J. I. Walter, and D. Vayenko (2015), Multiscale postseis-
846 mic behavior on a megathrust: The 2012 Nicoya earthquake, Costa Rica, *Geochemistry,*
847 *Geophysics, Geosystems*, 16(6), 1848–1864, doi:10.1002/2015GC005794.
- 848 Marone, C. J., C. H. Scholtz, and R. Bilham (1991), On the mechanics of earthquake
849 afterslip, *Journal of Geophysical Research: Solid Earth*, 96(B5), 8441–8452, doi:
850 10.1029/91JB00275.
- 851 Miller, S. A., C. Collettini, L. Chiaraluce, M. Cocco, M. Barchi, and B. J. P. Kaus
852 (2004), Aftershocks driven by a high-pressure CO₂ source at depth, *Nature*, 427(6976),
853 724–727, doi:10.1038/nature02251.
- 854 Minson, S. E., M. Simons, and J. L. Beck (2013), Bayesian inversion for finite fault earth-
855 quake source models I: theory and algorithm, *Geophysical Journal International*, 194(3),
856 1701–1726, doi:10.1093/gji/ggt180.
- 857 Miyazaki, S., P. Segall, J. Fukuda, and T. Kato (2004), Space time distribution of af-
858 terslip following the 2003 Tokachi-oki earthquake: Implications for variations in
859 fault zone frictional properties, *Geophysical Research Letters*, 31(6), L06,623, doi:
860 10.1029/2003GL019410.
- 861 Munekane, H. (2012), Coseismic and early postseismic slips associated with the 2011 off
862 the Pacific coast of Tohoku Earthquake sequence: EOF analysis of GPS kinematic time
863 series, *Earth, Planets and Space*, 64(12), 3, doi:10.5047/eps.2012.07.009.
- 864 Nur, A., and G. Mavko (1974), Postseismic Viscoelastic Rebound, *Science*, 183(4121),
865 204–206, doi:10.1126/science.183.4121.204.
- 866 Parzen, E. (1962), On Estimation of a Probability Density Function and Mode, *The Annals*
867 *of Mathematical Statistics*, 33(3), 1065–1076.
- 868 Peltzer, G., P. Rosen, F. Rogez, and K. Hudnut (1998), Poroelastic rebound along the Lan-
869 ders 1992 earthquake surface rupture, *Journal of Geophysical Research: Solid Earth*,
870 103(B12), 30,131–30,145, doi:10.1029/98JB02302.
- 871 Peng, Z., and P. Zhao (2009), Migration of early aftershocks following the 2004 Parkfield
872 earthquake, *Nature Geoscience*, 2, 877–881, doi:10.1038/ngeo697.
- 873 Perfettini, H., and J.-P. Avouac (2004), Postseismic relaxation driven by brittle creep:
874 A possible mechanism to reconcile geodetic measurements and the decay rate of af-
875 tershocks, application to the Chi-Chi earthquake, Taiwan, *Journal of Geophysical Re-*

- 876 *search: Solid Earth*, 109(B2), B02,304, doi:10.1029/2003JB002488.
- 877 Perfettini, H., and J.-P. Avouac (2007), Modeling afterslip and aftershocks following
878 the 1992 Landers earthquake, *Journal of Geophysical Research: Solid Earth*, 112(B7),
879 B07,409, doi:10.1029/2006JB004399.
- 880 Perfettini, H., and J. P. Avouac (2014), The seismic cycle in the area of the 2011
881 Mw9.0 Tohoku-Oki earthquake, *Journal of Geophysical Research: Solid Earth*, 119(5),
882 4469–4515, doi:10.1002/2013JB010697.
- 883 Perfettini, H., W. B. Frank, D. Marsan, and M. Bouchon (2018), A Model of Aftershock
884 Migration Driven by Afterslip, *Geophysical Research Letters*, 45(5), 2283–2293, doi:10.
885 1002/2017GL076287.
- 886 Pollitz, F. F., R. Burgmann, and P. Segall (1998), Joint estimation of afterslip rate and
887 postseismic relaxation following the 1989 Loma Prieta earthquake, *Journal of Geophysi-
888 cal Research: Solid Earth*, 103(B11), 26,975–26,992, doi:10.1029/98JB01554.
- 889 Pondrelli, S., S. Salimbeni, A. Morelli, G. Ekstrom, M. Olivieri, and E. Boschi (2010),
890 Seismic moment tensors of the April 2009, L’Aquila (Central Italy), earthquake se-
891 quence, *Geophysical Journal International*, 180(1), 238–242, doi:10.1111/j.1365-246X.
892 2009.04418.x.
- 893 Ragon, T., A. Sladen, and M. Simons (2018), Accounting for uncertain fault geometry in
894 earthquake source inversions - I: theory and simplified application, *Geophysical Journal
895 International*, 214(2), 1174–1190, doi:10.1093/gji/ggy187.
- 896 Rice, J., and A. L. Ruina (1983), *Stability of Steady Frictional Slipping*, vol. 50, doi:10.
897 1115/1.3167042.
- 898 Rosen, P. A., S. Henley, G. Peltzer, and M. Simons (2004), Update Repeat Orbit Interfer-
899 ometry Package Released, *EOS Transactions*, 85, 47–47, doi:10.1029/2004EO050004.
- 900 Ross, Z. E., C. Rollins, E. S. Cochran, E. Hauksson, J.-P. Avouac, and Y. Ben-Zion
901 (2017), Aftershocks driven by afterslip and fluid pressure sweeping through a fault-
902 fracture mesh, *Geophysical Research Letters*, 44(16), 2017GL074,634, doi:10.1002/
903 2017GL074634.
- 904 Salman, R., E. M. Hill, L. Feng, E. O. Lindsey, D. Mele Veedu, S. Barbot, P. Banerjee,
905 I. Hermawan, and D. H. Natawidjaja (2017), Piecemeal Rupture of the Mentawai Patch,
906 Sumatra: The 2008 Mw 7.2 North Pagai Earthquake Sequence, *Journal of Geophysical
907 Research: Solid Earth*, 122(11), 9404–9419, doi:10.1002/2017JB014341.
- 908 Scognamiglio, L., E. Tinti, and A. Michelini (2009), Real-Time Determination of Seismic
909 Moment Tensor for the Italian Region, *Bulletin of the Seismological Society of America*,
910 99(4), 2223–2242, doi:10.1785/0120080104.
- 911 Scuderi, M. M., and C. Collettini (2016), The role of fluid pressure in induced vs. trig-
912 gered seismicity: insights from rock deformation experiments on carbonates, *Scientific
913 Reports*, 6, 24,852, doi:10.1038/srep24852.
- 914 Segall, P. (2010), *Earthquake and Volcano Deformation*, Princeton University Press,
915 google-Books-ID: x6Fp4hMBTpYC.
- 916 Serpelloni, E., L. Anderlini, and M. E. Belardinelli (2012), Fault geometry, coseismic-
917 slip distribution and Coulomb stress change associated with the 2009 April 6, Mw 6.3,
918 L’Aquila earthquake from inversion of GPS displacements, *Geophysical Journal Interna-
919 tional*, 188(2), 473–489, doi:10.1111/j.1365-246X.2011.05279.x.
- 920 Sladen, A., H. Tavera, M. Simons, J. P. Avouac, A. O. Konca, H. Perfettini, L. Au-
921 din, E. J. Fielding, F. Ortega, and R. Cavagnoud (2010), Source model of the 2007
922 Mw 8.0 Pisco, Peru earthquake: Implications for seismogenic behavior of subduction
923 megathrusts, *Journal of Geophysical Research: Solid Earth*, 115(B2), B02,405, doi:
924 10.1029/2009JB006429.
- 925 Smith, B., and D. Sandwell (2004), A three-dimensional semianalytic viscoelastic model
926 for time-dependent analyses of the earthquake cycle, *Journal of Geophysical Research:
927 Solid Earth*, 109(B12), B12,401, doi:10.1029/2004JB003185.
- 928 Terakawa, T., A. Zoporowski, B. Galvan, and S. A. Miller (2010), High-pressure fluid at
929 hypocentral depths in the L’Aquila region inferred from earthquake focal mechanisms,

- 930 *Geology*, 38(11), 995–998, doi:10.1130/G31457.1.
- 931 Trasatti, E., C. Kyriakopoulos, and M. Chini (2011), Finite element inversion of DInSAR
932 data from the Mw 6.3 L'Aquila earthquake, 2009 (Italy), *Geophysical Research Letters*,
933 38(8), L08,306, doi:10.1029/2011GL046714.
- 934 Valoroso, L., L. Chiaraluce, D. Piccinini, R. Di Stefano, D. Schaff, and F. Waldhauser
935 (2013), Radiography of a normal fault system by 64,000 high-precision earthquake lo-
936 cations: The 2009 L'Aquila (central Italy) case study, *Journal of Geophysical Research:*
937 *Solid Earth*, 118(3), 1156–1176, doi:10.1002/jgrb.50130.
- 938 Vittori, E., P. D. Manna, A. M. Blumetti, V. Comerci, L. Guerrieri, E. Esposito, A. M.
939 Michetti, S. Porfido, L. Piccardi, G. P. Roberts, A. Berlusconi, F. Livio, G. Sileo,
940 M. Wilkinson, K. J. W. McCaffrey, R. J. Phillips, and P. A. Cowie (2011), Surface
941 Faulting of the 6 April 2009 Mw 6.3 L'Aquila Earthquake in Central Italy, *Bulletin of*
942 *the Seismological Society of America*, 101(4), 1507–1530, doi:10.1785/0120100140.
- 943 Volpe, M., A. Piersanti, and D. Melini (2012), Complex 3-D Finite Element modelling of
944 the 2009 April 6 L'Aquila earthquake by inverse analysis of static deformation, *Geo-*
945 *physical Journal International*, 188(3), 1339–1358, doi:10.1111/j.1365-246X.2011.
946 05330.x.
- 947 Volpe, M., S. Atzori, A. Piersanti, and D. Melini (2015), The 2009 L'Aquila earthquake
948 coseismic rupture: open issues and new insights from 3d finite element inversion of
949 GPS, InSAR and strong motion data, *Annals of Geophysics*, 58(2), S0221, doi:10.4401/
950 ag-6711.
- 951 Wang, L., S. Hainzl, G. Zoller, and M. Holschneider (2012), Stress- and aftershock-
952 constrained joint inversions for coseismic and postseismic slip applied to the 2004 M6.0
953 Parkfield earthquake, *Journal of Geophysical Research: Solid Earth*, 117(B7), B07,406,
954 doi:10.1029/2011JB009017.
- 955 Yano, T. E., G. Shao, Q. Liu, C. Ji, and R. J. Archuleta (2014), Coseismic and potential
956 early afterslip distribution of the 2009 Mw 6.3 L'Aquila, Italy earthquake, *Geophysical*
957 *Journal International*, 199(1), 23–40, doi:10.1093/gji/ggu241.
- 958 Zhu, L., and L. A. Rivera (2002), A note on the dynamic and static displacements from a
959 point source in multilayered media, *Geophysical Journal International*, 148(3), 619–627,
960 doi:10.1046/j.1365-246X.2002.01610.x.